9,400 years of cosmic radiation and solar activity from ice cores and tree rings

Friedhelm Steinhilber[a,1], Jose A. Abreu[a2], Jürg Beer[a], Irene Brunner[a], Marcus Christl[b], Hubertus Fischer[c], Ulla Heikkilä[d], Peter W. Kubik[b], Mathias Mann[a], Ken G. McCracken[e], Heinrich Miller[f], Hiroko Miyahara[g], Hans Oerter[f], and Frank Wilhelms[f]

[a]Swiss Federal Institute of Aquatic Science and Technology, Eawag, Überlandstrasse 133, 8600 Dübendorf, Switzerland; [b]Laboratory of Ion Beam Physics, Swiss Federal Institute of Technology Zurich, Schafmattstrasse 20, 8093 Zurich, Switzerland; [c]Climate and Environmental Physics, Physics Institute and Oeschger Centre for Climate Change Research, University of Bern, Sidlerstrasse 5, 3012 Bern, Switzerland; [d]Ulla Heikkilä, Australian Nuclear Science and Technology Organisation (ANSTO), Lucas Heights, North South Wales 2234, Australia; [e]Ken G. McCracken, Institute for Physical Science and Technology, University of Maryland, College Park, MD 20742; [f]Alfred Wegener Institute for Polar and Marine Research, Am Handelshafen 12, 27568 Bremerhaven, Germany; and [9]Institute for Cosmic Ray Research, University of Tokyo, 5-1-5 Kashiwanoha, Kashiwa 277-8582, Japan

Edited by Timothy Patterson, Carleton University, and accepted by the Editorial Board February 14, 2012 (received for review November 18, 2011)

Understanding the temporal variation of cosmic radiation and solar activity during the Holocene is essential for studies of the solar-terrestrial relationship. Cosmic-ray produced radionuclides, such as ^{10}Be and ^{14}C which are stored in polar ice cores and tree rings, offer the unique opportunity to reconstruct the history of cosmic radiation and solar activity over many millennia. Although records from different archives basically agree, they also show some deviations during certain periods. So far most reconstructions were based on only one single radionuclide record, which makes detection and correction of these deviations impossible. Here we combine different ^{10}Be ice core records from Greenland and Antarctica with the global ^{14}C tree ring record using principal component analysis. This approach is only possible due to a new high-resolution ^{10}Be record from Dronning Maud Land obtained within the European Project for Ice Coring in Antarctica in Antarctica. The new cosmic radiation record enables us to derive total solar irradiance, which is then used as a proxy of solar activity to identify the solar imprint in an Asian climate record. Though generally the agreement between solar forcing and Asian climate is good, there are also periods without any coherence, pointing to other forcings like volcanoes and greenhouse gases and their corresponding feedbacks. The newly derived records have the potential to improve our understanding of the solar dynamics and to quantify the solar influence on climate.

cosmogenic radionuclides | cosmic rays | solar modulation

Most of the cosmic ray particles reaching the Earth are produced outside the solar system during supernova explosions. Mainly two magnetic shields, the solar magnetic field and the geomagnetic field, modulate the cosmic ray flux approaching the Earth. Both shields vary in time, and so does the cosmic radiation at Earth. The weaker these fields, the higher is the cosmic ray intensity at Earth. Ionization chambers and neutron monitors have directly monitored the intensity of cosmic radiation since the 1930s (1). Prior to this time, no direct measurements exist, and cosmogenic radionuclides, which can be considered as a kind of a "natural neutron monitor," can be used as a proxy for cosmic radiation (2). In this context the two most commonly used radionuclides are ^{10}Be and ^{14}C. ^{10}Be and ^{14}C are produced in the Earth's atmosphere by nuclear reactions of cosmic ray particles with atmospheric nitrogen and oxygen (3) (Fig. 1). Thus, the production rates of these nuclides are directly related to the flux of the incoming cosmic ray particles. Although their production processes are very similar, their geochemical behavior in the Earth system is completely different (Fig. 1). ^{14}C enters the global carbon cycle, and therefore fluctuations of the atmospheric ^{14}C concentration (Fig. 2*B*) measured as Δ^{14}C in tree rings are damped, smoothed, and delayed relative to the ^{14}C production. The effect of the carbon cycle can be removed by inverse carbon cycle modeling. The resulting ^{14}C production rate (p^{14}C, Fig. 2 *C* and *D*) calculated with a box-diffusion carbon cycle model (4) is a better measure of the cosmic radiation, but it still contains a climate signal component due to unknown temporal changes of the carbon cycle and a memory effect of the production history. In contrast to ^{14}C, aerosol-borne ^{10}Be is removed from the atmosphere relatively fast within a few years and stored in natural archives such as polar ice sheets. Because of its short atmospheric residence time, ^{10}Be directly reflects cosmic ray intensity variations with almost no attenuation and a delay of 1–2 y. Uncertainties are introduced mainly on annual time scales by atmospheric mixing processes and wet and dry deposition from the atmosphere to the ice (5).

For the Holocene there are several radionuclide records with high temporal resolution: p^{14}C (Fig. 2 *C* and *D*) derived from Δ^{14}C measured in tree rings (Fig. 2*B*), and ^{10}Be from different ice cores from Greenland and Antarctica (Fig. 2 *A* and *D*). The high similarity between the two different radionuclides ^{14}C and ^{10}Be and the fact that the well known grand solar minima such as the Maunder and the Dalton minima are well represented in the radionuclide records (Fig. 2*D*) confirms that these records reflect primarily production changes caused by variations of the cosmic ray flux. However, closer inspection reveals that often, the shapes during these periods differ slightly in their details. Because the cosmic ray induced production changes are almost identical for ^{10}Be and ^{14}C, the differences observed in radionuclide records stored in geological archives are the result of so-called system effects. The term "system effects" is used here for all processes influencing the radionuclide signal (e.g., climate-induced transport and deposition changes, changes in the carbon cycle) other than cosmic ray-induced production (heliomagnetic and geomagnetic modulation). A prominent system effect, for example, is the variation of the snow accumulation rate, which directly affects the ^{10}Be concentration stored in the ice. To some extent system effects can be corrected. For example, snow accumulation effects can be partly removed by calculating ^{10}Be fluxes (concentration times snow accumulation rate). However, due to the combination of both wet and dry deposition on the total aerosol deposition, neither concentration nor fluxes are truly independent of accumulation rate (6). The determination of the snow accumulation

Author contributions: J.B. designed research; F.S., J.A.A., J.B., M.M., U.H., and K.G.M. performed research; F.S., H.F., H. Miller, H. Miyahara, H.O., and F.W. contributed new reagents/analytic tools; F.S., J.A.A., J.B., I.B., M.C., U.H., P.W.K., and M.M. analyzed data; and F.S. wrote the paper.

The authors declare no conflict of interest.

This article is a PNAS Direct Submission. T.P. is a guest editor invited by the Editorial Board.

[1]To whom correspondence should be addressed. E-mail: friedhelm.steinhilber@eawag.ch.

[2]Present address: Earth and Planetary Magnetism Group, Swiss Federal Institute of Technology Zurich, Institute of Geophysics, Sonneggstrasse 5, 8092 Zurich, Switzerland.

This article contains supporting information online at www.pnas.org/lookup/suppl/doi:10.1073/pnas.1118965109/-/DCSupplemental.

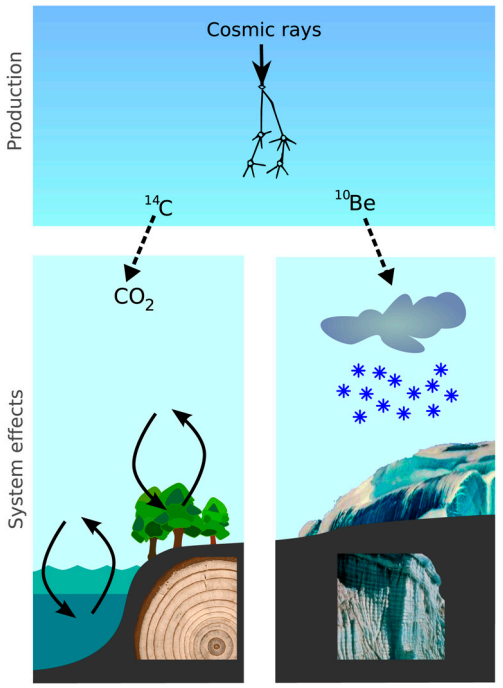

Fig. 1. Cartoon illustrating some basics of the radionuclides ^{14}C and ^{10}Be in the Earth's system. Both radionuclides are produced in a very similar way by nuclear reactions of cosmic ray particles with the atmospheric gases (3). After production, their fate is very different (system effects). ^{10}Be attaches to aerosols and is transported within a few years to ground (34). ^{14}C oxidizes to CO_2 and enters the global carbon cycle, exchanging between atmosphere, biosphere, and the oceans (4).

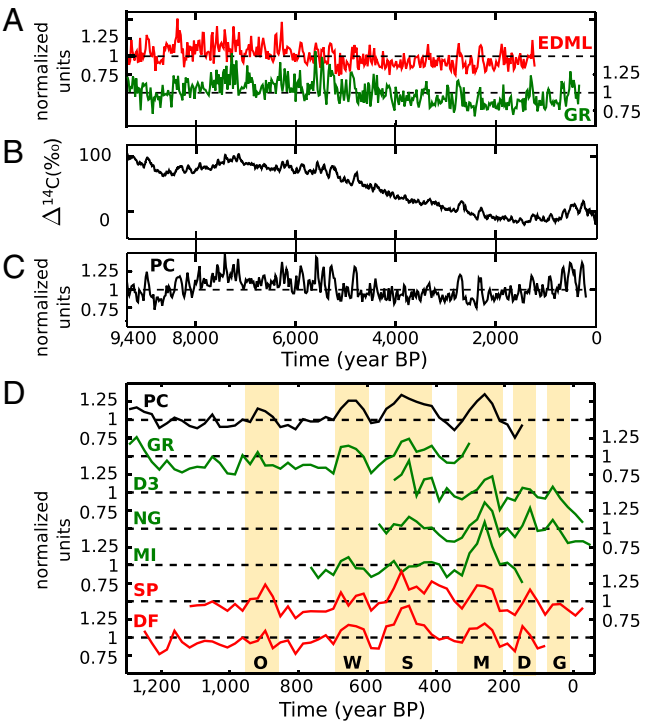

Fig. 2. Radionuclide records used for this study. ^{10}Be concentration records are green (Greenland) and red (Antarctica) and ^{14}C is black. Time is given as year before present (BP where present refers to 1950 AD). All records are mean normalized (divided by the mean) 22-year averages. (*A*) New ^{10}Be record from the EDML ice core (red) and of the existing ^{10}Be record from the GRIP (GR) ice core (green). The data are plotted on the time scales EDML1 (35) for EDML and GICC05 (36, 37) for GRIP. (*B*) $\Delta^{14}C$, the deviation of the atmospheric $^{14}C/^{12}C$ ratio from a standard value, measured in tree rings (14) and (*C*) ^{14}C production rate $p^{14}C$ (PC), calculated with a box-diffusion carbon cycle model (4) from $\Delta^{14}C$ (14) over the last 9,400 y. (*D*) ^{14}C production rate $p^{14}C$ (PC) and ^{10}Be concentrations for several available ice cores (GR: GRIP; D3: Dye-3; NG: NorthGRIP; MI: Milcent; SP: South Pole; DF: Dome Fuji) over the last 1,200 y. Grand solar minima are marked by yellow bands and capital letters: O: Oort, W: Wolf, S: Spörer, M: Maunder, D: Dalton, G: Gleissberg.

rate of an ice core is not trivial and is associated with additional uncertainties. In the polar regions of Greenland and Antarctica, snow accumulation rates have been rather stable during the Holocene so that ^{10}Be concentrations and fluxes yield similar results (*SI Appendix*, Section S7). For the sake of simplicity we use the concentrations below.

From this discussion it is obvious that individual radionuclide records may contain a significant system component which, if not eliminated, would be incorrectly attributed to variations of the cosmic radiation. In fact, system effects are probably the main reason for the observed differences between the existing reconstructions of cosmic radiation based on single radionuclide records only (7–10).

Results

Here we present a cosmic ray record for the past 9,400 y for which the system effects were minimized. This high-resolution and low-noise paleocosmic ray record is used to derive solar activity that in turn provides a powerful tool to search for the solar fingerprint in climate records.

Our approach first combines several hemispheric ^{10}Be records with the global ^{14}C record with high temporal resolution (Fig. 2 *A*, *C*, and *D* and Table 1) and then follows the study of Abreu, et al. (11) by using principal component analysis (PCA) to extract the common production signal. With PCA it is possible to disentangle the cosmic ray-induced production signal from the system effects. The successful separation is based on the assumption that the production signal is common to all records (correlated), whereas the system effects are different (uncorrelated) in each record. If system effects affected the radionuclide records spatially and temporarily in a similar way, PCA would "misinterpret" these effects as common variation which in turn would be wrongly attributed to cosmic radiation changes. However, it is known that climate effects differ spatially; hence it seems justified to assume that they affect the different radionuclide records from different hemispheres and archives differently.

The three main records of our reconstruction [^{10}Be from European Project for Ice Coring in Antarctica-Dronning Maid Land (EPICA-DML), Antarctica; ^{10}Be from European Greenland Ice Core Project (GRIP) (12, 13), Greenland; and global $p^{14}C$ from tree rings (14)] represent both hemispheres and are measured in different archives. These three records cover a time range from 1,194 to 9,400 y before present (BP) (*SI Appendix*, Section S1) and have a temporal resolution of a few years. The new ^{10}Be dataset from the EPICA-DML ice core consists of 1,846 data points with an average temporal resolution of about 4.5 y and therefore provides an essential part for the reconstruction. To homogenize the different records, 22-year averages are calculated for each individual record. Then PCA is applied to the 22-year averages. The first principal component explains 69% of the total variance (*SI Appendix*, Section S6). This is a striking result because it implies that the ^{14}C production changes throughout the Holocene are very similar to the ^{10}Be changes found in polar ice cores from the two different hemispheres. Again, because ^{10}Be and ^{14}C are produced in a very similar way and because system effects are not expected to correlate with the production signal, we conclude that the first principal component is the best representation of the global production rate and herewith of the cosmic ray intensity at Earth. The production signal obtained from ^{10}Be from GRIP and EPICA Dronning Maud

Table 1. Radionuclide records used in the study and their characteristics (3)

Record	Nuclide	Source	Time span (year before present)	Mean value used to normalize data in Fig. 2 (10^4 atoms/g)	Reference
INTCAL09	^{14}C	tree rings	9,400 to 150	1*	(14)
EDML†	^{10}Be	ice Antarctica	9,400 to 1,200	4.1	New
GRIP ‡	^{10}Be	ice Greenland	9,400 to 300	1.5	(12), (13)
Dye-3	^{10}Be	ice Greenland	526 to −35	1.1	(16)
Milcent	^{10}Be	ice Greenland	769 to 148	1.1	(17)
NorthGRIP	^{10}Be	ice Greenland	561 to −44	1.8	(15)
South Pole	^{10}Be	ice Antarctica	1,107 to −32	3.8	(19)
Dome Fuji	^{10}Be	ice Antarctica	1,255 to 75	9.4	(18)

*The ^{14}C production rate in the carbon cycle model is 1 (idealized units) for present day ($\Delta^{14}C = 0‰$). The global average ^{14}C production is approximately 2 atoms cm^{-2} s^{-1} (3).

†European Project for Ice Coring in Antarctica Dronning Maud Land area

‡European Greenland Ice Core Project

Land area (EDML) ice cores and ^{14}C from tree rings for the period 1,194–9,400 BP is extended to the present day by applying PCA to several other high-resolution ^{10}Be records from Greenland [NorthGRIP (15), Dye3 (16), Milcent (17)] and Antarctica [Dome Fuji (18), South Pole (19)], and to ^{14}C from tree rings (14). In this time interval the production signal is also dominant, explaining more than 67% of the total variance. The entire record is normalized to the two most recent 22-year averages centered in 1955 and 1977 AD (*SI Appendix*, Section S9). By combining several radionuclide records with PCA as done in this study, an assessment of the systematic uncertainty can be done. The common signal in radionuclide records describes about 70% of the variance, implying that the system effects cause the remaining 30%. These system effects are removed by using only the first principal component. The robustness of PCA was tested by applying a jackknife method, applying PCA to subsets of radionuclide records by leaving out single records. The jackknife uncertainty is on average 5% (*SI Appendix*, Section S8), which is significantly smaller than the large (greater than 50%) variations due to changes in solar activity between periods of low solar activity like the Maunder minimum (20) and of high solar activity like the past decades.

We note that there are several sources of systematic error that are not removed by PCA. These are (*i*) uncertainties in the time scales of the individual records, (*ii*) uncertainties in the production rate calculations of ^{10}Be and ^{14}C, (*iii*) the assumption that relative variations of ^{10}Be concentrations and ^{10}Be production rates are equal, (*iv*) uncertainty in the assumption of linear independence between production and system effects.

Variations on different time scales are evident in the final low-noise cosmic radiation (radionuclide production) record (Fig. 3 *B*, *C*, and *D*). A comparison with changes in the geomagnetic dipole field strength (21) (Fig. 3*A*) shows that the geomagnetic dipole shielding is the main cause of the observed multimillennial variability; the stronger the geomagnetic field, the lower is the cosmic radiation. On multidecadal to centennial time scales the cosmic radiation variations are mostly due to solar modulation (Fig. 3 *C* and *D*) as indicated by the coincidence of cosmic radiation maxima and grand solar (sunspot) minima like the Maunder minimum (Fig. 3*D*).

In a second step, we use the new low-noise cosmic radiation record to reconstruct total solar irradiance (TSI) by first removing the shielding effect of the geomagnetic field (3) (Fig. 3*A*) and then applying the procedure described in refs. 22–24 (*SI Appendix*, Section S10). The wavelet coherence between TSI of this study and two other recent TSI reconstructions (22, 25) based on single radionuclide records show agreement in the low-frequency part (periods longer than 100 y) and differences in the high-frequency part (periods shorter than 100 y) (*SI Appendix*, Section S13). This finding indicates that the PCA has indeed reduced the high-frequency noise present in the individual single radionuclide records.

In a last step, TSI is compared with the δ^{18}O record from Dongge cave, China, supposedly reflecting variations in precipitation amount related to changes in the Asian monsoon (AM) (26) (Fig. 4).

Note, however, that a recent climate modeling study (27) did not find a correlation between δ^{18}O in Chinese precipitation and the amount of precipitation over the Holocene. However, the study (27) showed that changes in monsoon are related to changes in δ^{18}O, although not via variations in the amount of precipitation.

Climate records have been often compared with Δ^{14}C as a proxy of solar activity. The Dongge Cave record has been previously compared with Δ^{14}C (21). As discussed above, Δ^{14}C is

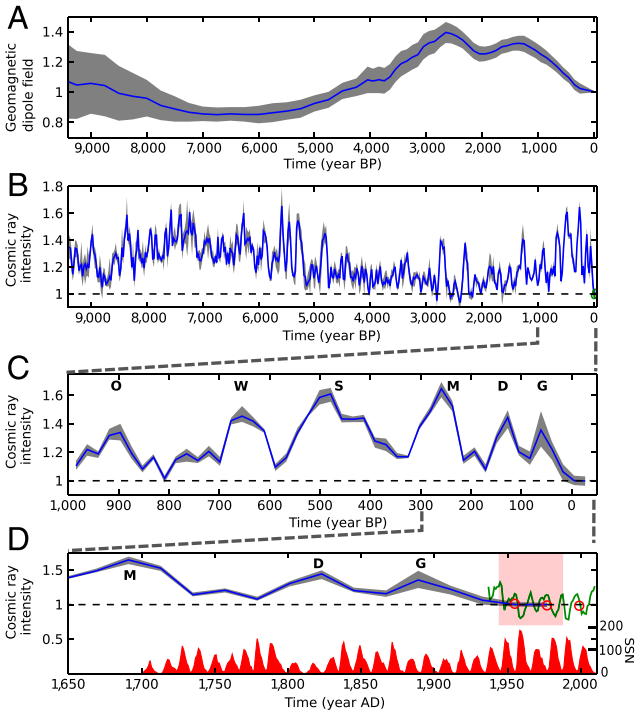

Fig. 3. (*A*) Geomagnetic dipole field strength relative to today (21). (*B*) Cosmic radiation based on the first principal component of several radionuclide records, 22-year averages, over the last 8,000 y. Time is given as year BP. The gray band represents the standard deviation of the individual radionuclide records without applying PCA (*SI Appendix*, Section S8). The black dashed line represents the average cosmic ray intensity for 1944–1988 AD. (*C*) Same as (*B*), but zoom-in of the past millennium. Capital letters mark grand solar minima: O: Oort, W: Wolf, S: Spörer, M: Maunder, D: Dalton, G: Gleissberg. (*D*) Same as (*C*), but zoom-in of the past 350 y. Time is given as year AD. Red circles and green curve are 22-year averages and yearly averages of cosmic ray intensity calculated with (3) using the solar modulation potential (38) obtained from neutron monitor and ionization chamber data (*SI Appendix*, Section S9). At the bottom the annual sunspot number is plotted (39).

not directly showing the solar forcing signal but a solar and geomagnetic production signal filtered by the carbon cycle system, which leads to a frequency dependent attenuation of the amplitude and a phase shift. Thus, a repetition using the solar activity record derived in our study appears to be justified. This climate record was chosen for two reasons: First, it is one of the few accurately dated climate records with high resolution that covers a similar period as the derived TSI. Second, it is a good example to demonstrate how to detect a solar signal in a climate record. The climate record has a large long-term trend due to orbital forcing, which we removed by subtracting the linear trend and applying a 2,000-year high-pass filter. We used the same data processing (subtracting the linear trend and applying a 2,000-year high-pass filter) for TSI.

We emphasize that changes in TSI are phase-locked with changes in solar spectral irradiance and with other changes related with solar activity, and therefore here we cannot distinguish between these different solar forcings. Hence, in this context TSI is taken as a proxy of solar activity, which is the reason we use the term solar activity instead of TSI in the following discussion.

The Pearson correlation between solar activity and AM is $R = -0.29$, meaning, during periods of low solar activity the AM strength has been weaker (higher $\delta^{18}O$) (Fig. 4*A*). Despite being significantly different from zero ($p < 10^{-6}$), this correlation, however, can only explain 10% in the total decadal to centennial variance in the AM record. We did a correlation analysis and found that the strongest correlation is found for a slightly negative lag (22 y), which is consistent with no lag within the uncertainty (*SI Appendix*, Section S12). The power spectrum of solar activity (*SI Appendix*, Section S11) shows significant periodicities ($p < 0.05$) already known from individual ^{14}C and ^{10}Be records such as the de Vries cycle (around 210 y), the Eddy cycle (around 1,000 y) (28), and an unnamed cycle at approximately 350 y, as well as other less significant unnamed cycles at approximately 500 and 710 y. These periodicities, although not significant, are also found in the Asian climate (*SI Appendix*, Section S11). The wavelet spectrum of solar activity (Fig. 4*B*) shows that the amplitudes

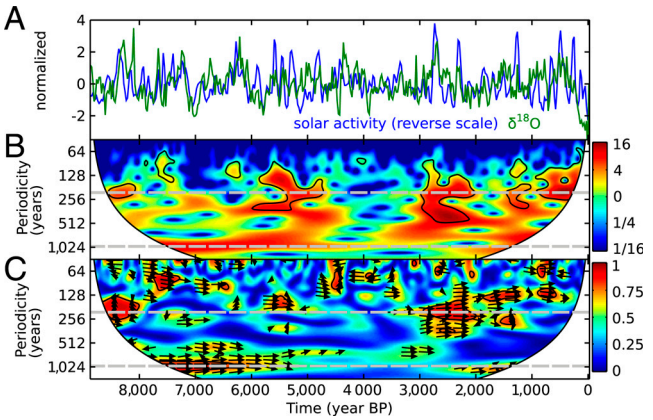

Fig. 4. Comparison of solar activity (total solar irradiance [TSI]) in blue and $\delta^{18}O$ from Dongge cave, China, in green representing changes of the Asian climate. possibly the Asian monsoon (AM) (low $\delta^{18}O$ corresponds to strong AM monsoon and vice versa). TSI has been reconstructed from the cosmic ray intensity reconstruction (*SI Appendix*, Section S10). Both records have been normalized (subtraction of mean value and division by the standard deviation), linearly detrended and high-pass filtered with 2,000 y. (*A*) Time series of solar activity (TSI) and $\delta^{18}O$. Solar activity (TSI) is plotted on a reversed scale. (*B*) Wavelet of solar activity (TSI). De Vries cycle at approximately 210 y and Eddy cycle at approximately 1,000 y are marked with horizontal, gray dashed lines. Black boundaries mark 95% significance level. (*C*) Wavelet coherence of solar activity (TSI) and $\delta^{18}O$. De Vries cycle at approximately 210 y and Eddy cycle at approximately 1,000 y are marked with horizontal, gray dashed lines. Arrows pointing to the right indicate that the records are in phase. Black boundaries mark the 95% significance level.

of these periodicities have varied in time, that is, the de Vries cycle amplitude has varied with a period of about 2,200 y, called the Hallstatt cycle (29). The largest amplitudes of the de Vries cycle are found during Hallstatt cycle minima centered at approximately 8,200; 5,500; 2,500; and 500 BP. Comparison of the time series of solar activity and its wavelet spectrum (Fig. 4 *A* and *B*) show that grand solar minima occur preferentially at minima of the de Vries cycles (note that solar activity is plotted on a reversed scale in Fig. 4*A*). Comparison of the time series of solar activity and climate (Fig. 4*A*) and their wavelet coherence (Fig. 4*C*) shows that in general during the Hallstatt cycle minima of solar activity (again characterized by large de Vries cycle amplitudes and a frequent occurrence of grand solar minima) the AM is weaker. However, there is some discrepancy during the Hallstatt cycle minima between 5,000 and 6,000 BP and in the past 1,500 y. During these periods the wavelet coherence for the periodicity of the de Vries cycle (around 210 y) is low, although several grand solar minima are visible. A similar pattern is visible at the Eddy periodicity (around 1,000 y), which has high power in the wavelet coherence, except in the period 3,000 to 5,000 BP. Such temporal differences are expected because the Sun is not the only driver of the climate system. Other forcing factors such as volcanic aerosols and greenhouse gases have changed in time, obscuring temporally the solar fingerprint.

Conclusions

We combined a new ^{10}Be record from Dronning Maud Land, Antarctica, comprising more than 1,800 data points with several other already existing radionuclide records (^{14}C from tree rings and ^{10}Be analyzed in polar ice cores of Greenland and Antarctica) covering the Holocene. Using principal component analysis, we separated the common radionuclide production signal due to solar and geomagnetic activity from the system effects signal due to the different transport and deposition processes. The common signal represents a low-noise record of cosmic radiation, particularly for high frequencies, compared to earlier reconstructions, which are only based on single radionuclide records. On the basis of this record, we then derived a reconstruction of total solar irradiance for the Holocene, which overall agrees well with two existing records but shows less high-frequency noise. A comparison of the derived solar activity with a record of Asian climate derived from $\delta^{18}O$ in a Chinese stalagmite reveals a significant correlation. The correlation is remarkable because the Earth's climate has not been driven by the Sun alone. Other forcings like volcanoes, greenhouse gas concentrations, and internal variability also have played an important role. To quantify the solar influence on the Earth's climate and to distinguish between the different forcings, climate model simulations are required for the Holocene, employing the new dataset of total solar irradiance. The dataset will be available online at the National Oceanic and Atmospheric Administration paleo server (http://www.ncdc.noaa.gov/paleo/forcing.html).

Materials and Methods

Records Used in This Study. Table 1 summarizes the characteristics of the records used in this study. We applied a decay correction to the ^{10}Be records, using a half-life of (1.387 ± 0.012) million years (30, 31). The production rate p^{14}C from the atmospheric ^{14}C concentrations as measured in tree rings (14) has been calculated with a box-diffusion carbon cycle model (4).

^{10}Be EDML Record. The EDML ice core, located on the high plateau of the Atlantic sector of the East Antarctic ice sheet in Antarctic Dronning Maud Land, Antarctica, was drilled within the EPICA framework (32). The ^{10}Be record used covers the period from 1,193 to 9,400 BP. The chemical preparation of the ^{10}Be samples was done at Eawag in Dübendorf, Switzerland. First the ice was cut into samples of 25 cm length, corresponding to an average time resolution of about 4.5 y. Then the ice was melted in a microwave oven, mixed with 0.125 mg of ^{9}Be carrier, and passed through a cation ion exchange resin. The chemical preparation was done in the same way as for the ^{10}Be samples from the GRIP ice core (12, 13). The samples were measured

at the accelerator mass spectrometry (AMS) facility of Ion Beam Physics group at Swiss Federal Institute of Technology Zurich, Switzerland. The typical AMS uncertainty is 5%. The results were normalized to the ETH standard S555N (33).

Computational Analysis. The radionuclide records were combined into one using principal component analysis (PCA) to obtain a record covering the entire period of interest. First we divided each record into a series of consecutive 22-year intervals, with the interval centers being the same for all records. The data points in each interval were averaged, and this average was assigned to the central age. The principal components (PCs) were built from eight blocks of records with each block containing two to six individual radionuclide records (*SI Appendix*, Section S6). The first PC describes most of the total variance and is interpreted as the production signal due to solar and geomagnetic modulation. The first PC of one block is then normalized in such a way that its mean is equal to the mean of the first PC of the previous block in the overlapping interval covered by the two blocks. Note that we changed only the mean but not the variance. Finally, the curves of the eight blocks are combined to represent the common production signal variation. The robustness was tested with a jackknife method by repeating PCA and systematically leaving out one radionuclide record.

ACKNOWLEDGMENTS. We acknowledge financial support by National Centre of Competence in Research climate, Swiss climate research, and by the Swiss National Science Foundation under Grant CRSI122-130642 (Future and Past Solar Influence on the Terrestrial Climate). This work is a contribution to the European Project for Ice Coring in Antarctica (European Project for Ice Coring in Antarctica), a joint European Science Foundation/European Commission scientific program, funded by the European Union and by national contributions from Belgium, Denmark, France, Germany, Italy, the Netherlands, Norway, Sweden, Switzerland, and the United Kingdom. The main logistic support was provided by L'Institut polaire français Paul-Emile Victor and Programma Nazionale di Ricerche in Antartide (at Dome C) and Alfred-Wegener Institute (at Dronning Maud Land). This is EPICA publication no. 282.

1. McCracken KG, Beer J (2007) Long-term changes in the cosmic ray intensity at Earth, 1428–2005. *J Geophys Res-Space* 112:A10101.
2. Beer J (2000) Neutron monitor records in broader historical context. *Space Sci Rev* 107–119.
3. Masarik J, Beer J (2009) An updated simulation of particle fluxes and cosmogenic nuclide production in the Earth's atmosphere. *J Geophys Res-Atmos* 114:D11103.
4. Siegenthaler U (1983) Uptake of excess CO_2 by an outcrop-diffusion model of the ocean. *J Geophys Res-Oc Atm* 88:3599–3608.
5. Beer J, McCracken KG, Abreu J, Heikkilä U, Steinhilber F (2011) Cosmogenic radionuclides as an extension of the neutron monitor era into the past: potential and *Limitations Space Sci Rev.* ONLINE FIRST ARTICLE.
6. Fischer H, Siggaard-Andersen ML, Ruth U, Rothlisberger R, Wolff E (2007) Glacial/interglacial changes in mineral dust and sea-salt records in polar ice cores: Sources, transport, and deposition. *Rev Geophys* 45:RG1002.
7. Solanki SK, Usoskin IG, Kromer B, Schussler M, Beer J (2004) Unusual activity of the Sun during recent decades compared to the previous 11,000 years. *Nature* 431:1084–1087.
8. Steinhilber F, Abreu J, Beer J (2008) Solar modulation during the Holocene. *Astrophysics and Space Sciences Transactions* 4:1–6, (http://www.astrophysics-and-space-sciences-transactions.net/).
9. Usoskin IG, Solanki SK, Kovaltsov GA (2007) Grand minima and maxima of solar activity: new observational constraints. *Astron Astrophys* 471:301–309.
10. Vonmoos M, Beer J, Muscheler R (2006) Large variations in Holocene solar activity: Constraints from Be-10 in the Greenland Ice Core Project ice core. *J Geophys Res-Space* 111:A10105.
11. Abreu JA, Beer J, Steinhilber F, Christl F, Kubik PW (2012) ^{10}Be in Ice Cores and ^{14}C in tree rings: separation of production and climate effects. *Space Sci Rev* ONLINE FIRST ARTICLE.
12. Muscheler R, et al. (2004) Changes in the carbon cycle during the last deglaciation as indicated by the comparison of Be-10 and C-14 records. *Earth Planet Sc Lett* 219:325–340.
13. Yiou F, et al. (1997) Beryllium 10 in the Greenland Ice Core Project ice core at Summit, Greenland. *J Geophys Res-Oceans* 102:26783–26794.
14. Reimer PJ, et al. (2009) Intcal09 and Marine09 radiocarbon age calibration curves, 0–50,000 Years Cal Bp. *Radiocarbon* 51:1111–1150.
15. Berggren AM, et al. (2009) A 600-year annual Be-10 record from the NGRIP ice core, Greenland. *Geophys Res Lett* 36:L11801.
16. Beer J, Tobias S, Weiss N (1998) An active sun throughout the Maunder Minimum. *Sol Phys* 181:237–249.
17. Beer J, et al. (1985) Accelerator measurements of Be-10—the 11 Year solar-cycle from 1180–1800 Ad. *Nucl Instrum Meth B* 10-1:415–418.
18. Horiuchi K, et al. (2008) Ice core record of Be-10 over the past millennium from Dome Fuji, Antarctica: a new proxy record of past solar activity and a powerful tool for stratigraphic dating. *Quat Geochronol* 3:253–261.
19. Raisbeck GM, Yiou F, Jouzel J, Petit JR (1990) Be-10 and Delta-H-2 in polar ice cores as a probe of the solar variability influence on climate. *Philos T R Soc A* 330:463–470.
20. Eddy JA (1976) The Maunder minimum. *Science* 192:1189–1202.
21. Knudsen MF, et al. (2008) Variations in the geomagnetic dipole moment during the Holocene and the past 50 kyr. *Earth Planet Sc Lett* 272:319–329.
22. Steinhilber F, Beer J, Frohlich C (2009) Total solar irradiance during the Holocene. *Geophys Res Lett* 36:L19704.
23. Steinhilber F, Abreu JA, Beer J, McCracken KG (2010) Interplanetary magnetic field during the past 9300 years inferred from cosmogenic radionuclides. *J Geophys Res-Space* 115:A01104.
24. Frohlich C (2009) Evidence of a long-term trend in total solar irradiance. *Astron Astrophys* 501:L27–U508.
25. Vieira LEA, Solanki SK, Krivova N, Usoskin I (2011) Evolution of the solar irradiance during the Holocene. *Astron Astrophys* 531:A6.
26. Wang YJ, et al. (2005) The Holocene Asian monsoon: links to solar changes and North Atlantic climate. *Science* 308:854–857.
27. LeGrande AN, Schmidt GA (2009) Sources of Holocene variability of oxygen isotopes in paleoclimate archives. *Clim Past* 5:441–455.
28. Abreu JA, Beer J, Ferriz-Mas A (2010) Past and future solar activity from cosmogenic radionuclides. Astronomical Society of the Pacific Conference Series: SOHO-23: understanding a peculiar solar minimum. *SOHO-23: understanding a peculiar solar minimum*, eds SR Cranmer, JT Hoeksema, and JL Kohl 428 (Astronomical Society of the Pacific Conference Series (2010), UT), pp 287–295.
29. Damon PE, Sonett CP (1991) Solar and terrestrial componants of the atmospheric ^{14}C variation spectrum. *The Sun in Time*, eds CP Sonett, MS Giampapa, and S Matthews (University of Arizona Press, Tucson), pp 360–388.
30. Korschinek G, et al. (2010) A new value for the half-life of Be-10 by heavy-ion elastic recoil detection and liquid scintillation counting. *Nucl Instrum Meth B* 268:187–191.
31. Chmeleff J, von Blanckenburg F, Kossert K, Jakob D (2010) Determination of the Be-10 half-life by multicollector ICP-MS and liquid scintillation counting. *Nucl Instrum Meth B* 268:192–199.
32. Epica Community Members (2006) One-to-one coupling of glacial climate variability in Greenland and Antarctica. *Nature* 444:195–198.
33. Kubik PW, Christl M (2010) Be-10 and Al-26 measurements at the Zurich 6 MV Tandem AMS facility. *Nucl Instrum Meth B* 268:880–883.
34. Heikkila U, Beer J, Feichter J (2009) Meridional transport and deposition of atmospheric Be-10. *Atmos Chem Phys* 9:515–527.
35. Ruth U, et al. (2007) EDML1: A chronology for the EPICA deep ice core from Dronning Maud Land, Antarctica, over the last 150,000 years. *Clim Past* 3:475–484.
36. Vinther BM, et al. (2006) A synchronized dating of three Greenland ice cores throughout the Holocene. *J Geophys Res-Atmos* 111:D13102.
37. Rasmussen SO, et al. (2006) A new Greenland ice core chronology for the last glacial termination. *J Geophys Res-Atmos* 111:D06102.
38. Usoskin IG, Bazilevskaya GA, Kovaltsov GA (2011) Solar modulation parameter for cosmic rays since 1936 reconstructed from ground-based neutron monitors and ionization chambers. *J Geophys Res-Space* 116:A02104.
39. SIDC-Team (2012), The International Sunspot Number Monthly Report on the International Sunspot Number, online catalogue, http://www.sidc.be/sunspot-data/.

Supporting information

S1. Records used in this study

*Table S1: Radionuclide records used in the study and their characteristics. *The ^{14}C production rate in the carbon cycle model is 1 (idealized units) for present day ($\Delta^{14}C$=0 ‰). The global average ^{14}C production is approximately 2 atoms cm^{-2} s^{-1} (1).*

Record	Nuclide	Source	Time span (year BP)	Temporal resolution (years)	Ref.	Mean value to normalize data in Fig. 2 (10^4 atoms/g)
INTCAL09	^{14}C	Tree-rings	9400 to 150	5-10	(2)	1*
EDML	^{10}Be	Ice Antarctica	9400 to 1200	4-5	**New**	4.1
GRIP	^{10}Be	Ice Greenland	9400 to 300	4-5	(3), (4)	1.5
Dye-3	^{10}Be	Ice Greenland	526 to -35	1	(5)	1.1
Milcent	^{10}Be	Ice Greenland	769 to 148	3-4	(6)	1.1
NorthGRIP	^{10}Be	Ice Greenland	561 to -44	1	(7)	1.8
South Pole	^{10}Be	Ice Antarctica	1107 to -32	~8	(8)	3.8
Dome Fuji	^{10}Be	Ice Antarctica	1255 to 75	10	(9)	9.4

S2. Description of the ^{10}Be EDML record

The EDML ice core was drilled within the framework of the European Project for Ice Coring in Antarctica (EPICA) located at Dronning Maud Land (DML) (75 0.10' S, 0 4.07' E, 2882 m), Antarctica(10). The ^{10}Be record used herein covers the period from 1,193 BP to 9,400 BP (corresponding to a depth range from 113 m to 585 m). The processing of the EDML ice core took place at Alfred-Wegener Institute / Bremerhaven in a joint action by the institutes involved in EPICA.

The chemical preparation of the ^{10}Be samples was done at Eawag in Dübendorf/Switzerland. The ice was cut into samples of 25 cm length (about 100g of ice per sample), corresponding to an average sample temporal resolution of about 4.5 years throughout the Holocene. Then the ice was melted in a microwave oven, mixed with 0.125 mg of ^{9}Be carrier and passed through a cation ion exchange resin. We did not use any filters. The chemical preparation was done in the same way as for the ^{10}Be samples from the GRIP ice core (see (3), (4)). The ^{10}Be samples were measured at the accelerator mass spectrometer (AMS) facility of ETH Zurich, Switzerland. The typical AMS counting uncertainty of the ice core samples is about 5 %. The results were normalized to the ETH standard S555N(11).

We use the time scale called EDML1(12). ^{10}Be fluxes are obtained by multiplying the ^{10}Be concentrations with the corresponding accumulation rates from Ref. (12).

S3. Remarks to ^{10}Be measurements

The different ^{10}Be records, which were used in this study, have been normalized to different AMS standards. Because we are interested in the relative variations only, we normalized the records to their respective mean values.

S4. ^{10}Be half-life correction

We applied a decay correction to the ^{10}Be records, using a half-life of (1.387+-0.012) million years ((13, 14)).

S5. ^{14}C production rate

We applied a box-diffusion carbon cycle model (15) to calculate the production rate p14C from the atmospheric ^{14}C concentrations as measured in tree rings (2). Thereby we assumed that the carbon cycle has been stable throughout the Holocene.

S6. Determination of common production rate (cosmic ray intensity) with principal component analysis (PCA)

The individual radionuclide records used here cover different time periods. In order to remove the system effects (see article) from the records we applied PCA instead of using mean values. A prerequisite of PCA is that the input data have the same sample resolution and cover the same time interval. First we divided each record into a series of consecutive 22-year intervals with the interval centers being the same in all records. The data points in each interval were averaged and this average was assigned to the central age. The principal components (PCs) were built from eight blocks (Table S2) of records with each block containing between 2 to 6 individual radionuclide records.

Table S2: Blocks of records used in PCA and for determining the common production rate (cosmic ray intensity). Time series and resulting common cosmic ray intensity are shown for the individual blocks 1-8 in Figures S1-S8. Year BP=before present (1950AD). 1.PC=First principal component.

Block number	Records used (number of records)	Time interval in PCA (year BP)	Used time interval (year BP)	Total variance described by 1.PC	Normalization period (year BP)
1	Dye-3, NorthGRIP, South Pole (3)	534 to -38	72 to -38	76%	6 to -38 (1944-1988 AD)
2	Dye-3, NorthGRIP, South Pole, Dome Fuji (4)	534 to 72	138 to 72	72%	544 to 72
3	Dye-3, NorthGRIP, South Pole, Dome Fuji, INTCAL09-p14c, Milcent (6)	534 to 149	534 to 138	67%	544 to 138
4	South Pole, Dome Fuji, INTCAL09-p14c, Milcent, GRIP (5)	776 to 292	776 to 534	72%	544 to 292
5	GRIP, Dome Fuji, South Pole, INTCAL09-p14c (4)	1128 to 292	1128 to 776	82%	765 to 292
6	GRIP, Dome Fuji, INTCAL09-p14c (3)	1260 to 292	1194 to 1128	88%	1128 to 292
7	GRIP, p14C (2)	9400 to 292	Used for normalization only (see note below)	77%	1260 to 292
8	EDML, GRIP, INTCAL09-p14c (3)	9400 to 1194	9400 to 1194	69%	2206 to 1194

Before applying PCA all records were standardized by subtracting the mean and dividing by the standard deviation of the individual records. PCA gives as many principal components as input records are used. We consider only the first principal component, which describes most of the total variance in all records shown as percentages of the total variance in Table S2. Because the records used as input data fort PCA were standardized the PCs are also in standardized units. To obtain

physical units, the first PC was first multiplied with the standard deviation of the individual records and second the mean of the individual records was added. Then all records were divided by their mean value. These records in each block show the common signal of those records in units relative to their individual mean. We calculated the mean value of these records which is the "mean common signal" of the corresponding block.

The mean common signals are then normalized in such a way that the mean signal is equal to the signal of the previous block in their overlapping interval (Table S2, Figures S1-S8). This was done by dividing the block by its mean in the overlapping interval with the previous block and by multiplying the block with the mean of the previous block in the overlapping interval. The blocks are based on different datasets and cover different time periods and therefore the variance is not equal in the individual blocks. This is the reason that we only adjust the mean of a block with the former block but not the variance. The variances are compared in Table S3. The normalization periods for consecutive blocks are shown in the last column of Table S2. Block 1 has been normalized in such a way that the average signal in the period 1944-1988 is 1. The normalization periods for blocks 2-7 are the entire overlapping interval with the former block. Block 8 was normalized with Block 7 over 1000 years in the youngest part of the overlapping period. Finally mean curves are calculated for each block. The mean curves of the eight blocks are combined to represent the common production signal variation (cosmic ray intensity).

Block number	Records used (number of records)	Variance in overlapping interval (normalized units) (former block, this block)	Ratio former block/this block
1	Dye-3, NorthGRIP, South Pole (3)		
2	Dye-3, NorthGRIP, South Pole, Dome Fuji (4)	0.17, 0.175	0.97
3	Dye-3, NorthGRIP, South Pole, Dome Fuji, INTCAL09-p14c, Milcent (6)	0.18, 0.17	1.02
4	South Pole, Dome Fuji, INTCAL09-p14c, Milcent, GRIP (5)	0.15, 0.14	1.1
5	GRIP, Dome Fuji, South Pole, INTCAL09-p14c (4)	0.15, 0.16	0.89
6	GRIP, Dome Fuji, INTCAL09-p14c (3)	0.16, 0.16	0.97
7	GRIP, p14C (2)	0.16, 0.16	1.0
8	EDML, GRIP, INTCAL09-p14c (3)	0.11, 0.09	1.18

Table S3: Comparison of variances in the overlapping intervals of the block and the former block.

Note, that block 6 overlaps with block 8, but the overlap interval consists of only three data points from the years 1260-1194BP which is not long enough for an accurate normalization. Hence we did not use block 6 to normalize block 8. We introduced block 7 based only on GRIP ^{10}Be data and p^{14}C. This block was normalized with block 6, and then used to normalize block 8. Block 7 and

block 8 cover the same time span back to 9400 BP, but because block 8 considers also EDML ^{10}Be, it is a more robust record of cosmic ray intensity over the entire period.

The following figures illustrate how the records were normalized and combined to obtain the 9400-year record. Every figure has three panels. In the top panel the raw 22-year averages of the various radionuclide records used for the time interval of the block are shown. The middle panel shows the common average first principal component (1.PC) using all records and leaving out one record (jackknife method) together with the percentage described by the 1.PC (eigenvalue of the 1.PC). The bottom panel shows how the corresponding block agrees with the previous block within the overlapping interval to build the composite. The redish intervals mark the periods used to normalize the two corresponding blocks.

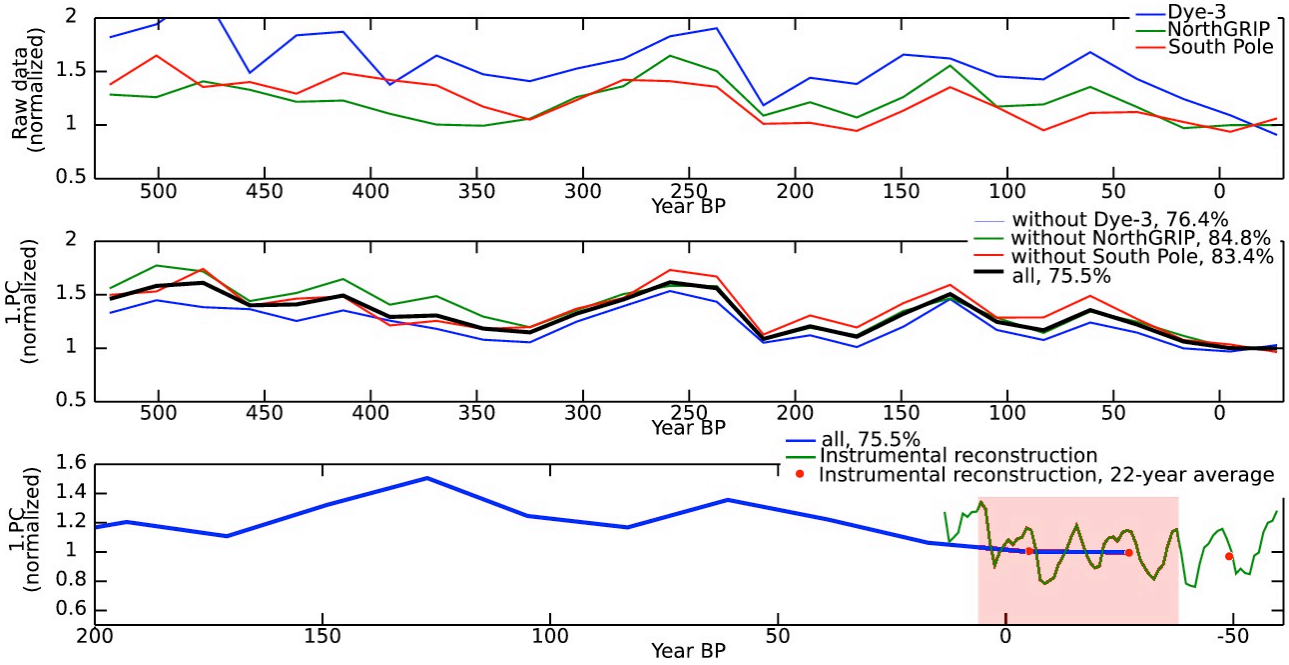

Figure S1 Normalization of block 1. The redish interval is used as normalization period (for details see section 9 and Figure S11). Instrumental reconstruction based on neutron monitor and ionization chamber data (see section S9 for details).

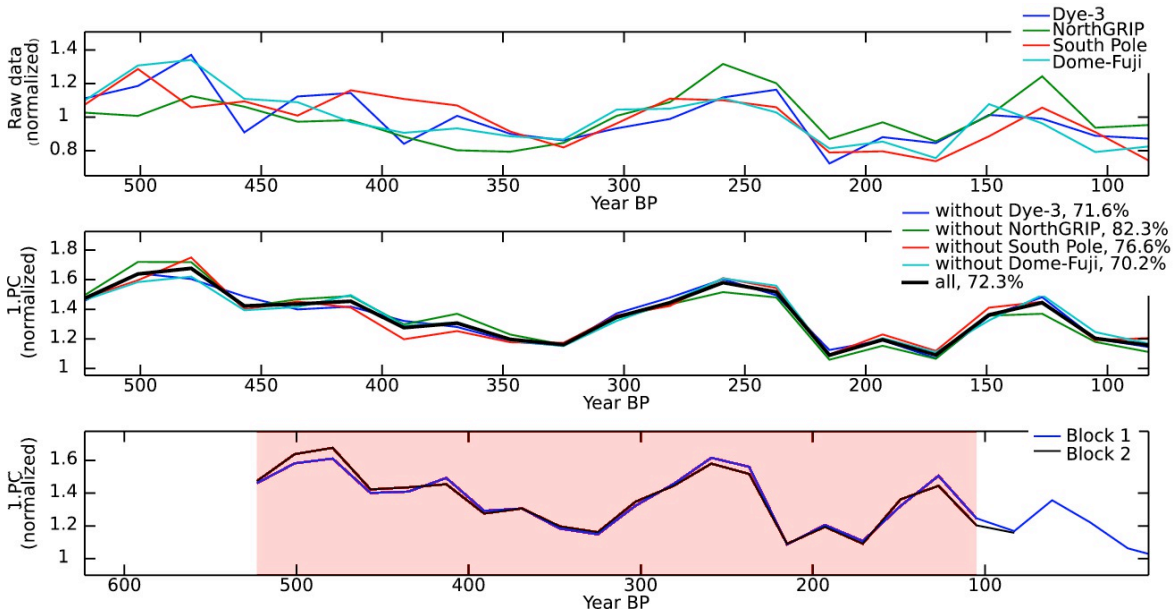

Figure S2 Normalization of block 2. The redish interval is used as normalization period.

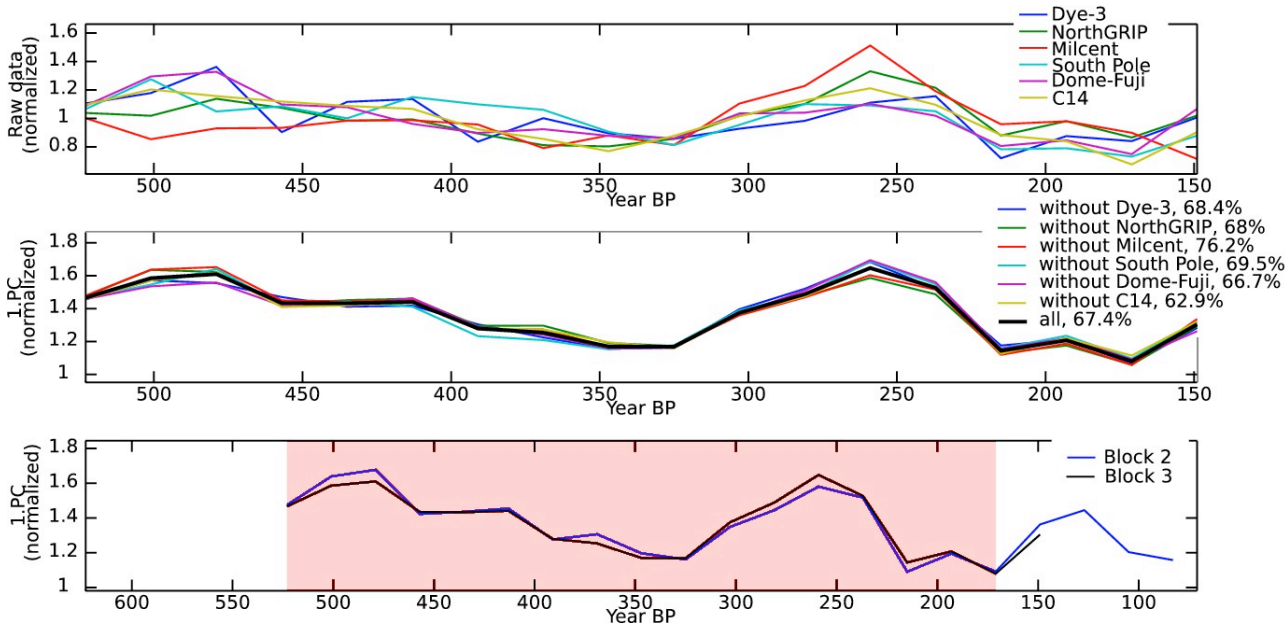

Figure S3 Normalization of block 3. The redish interval is used as normalization period.

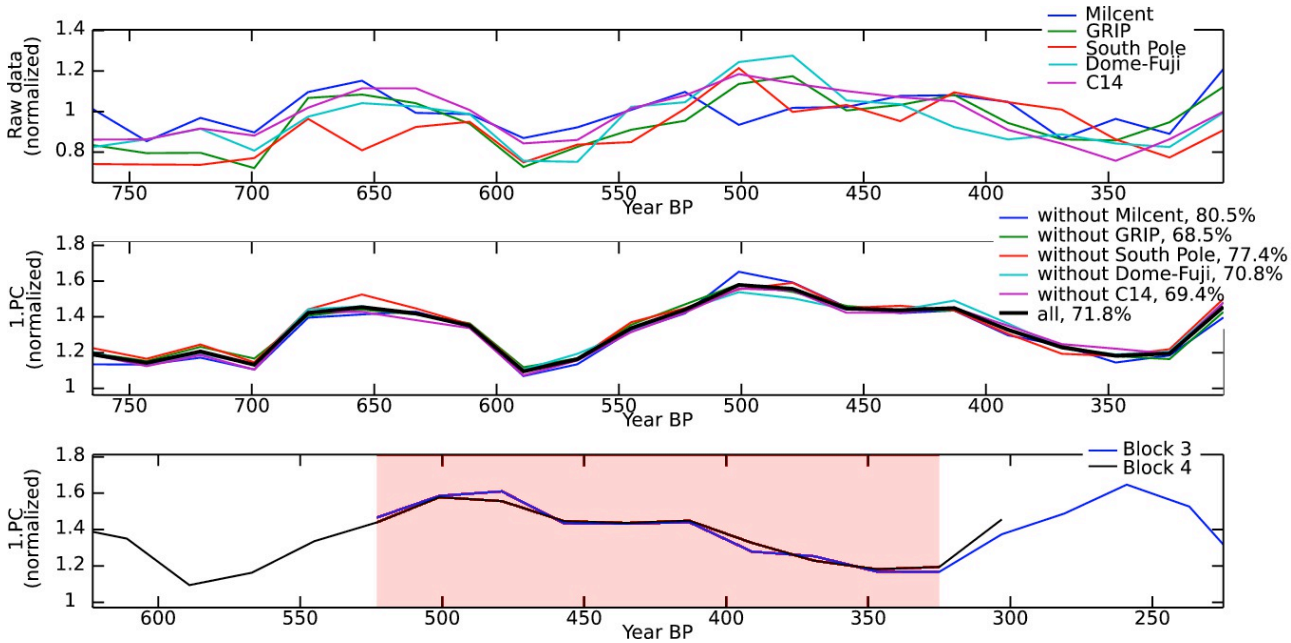

Figure S4 Normalization of block 4. The redish interval is used as normalization period.

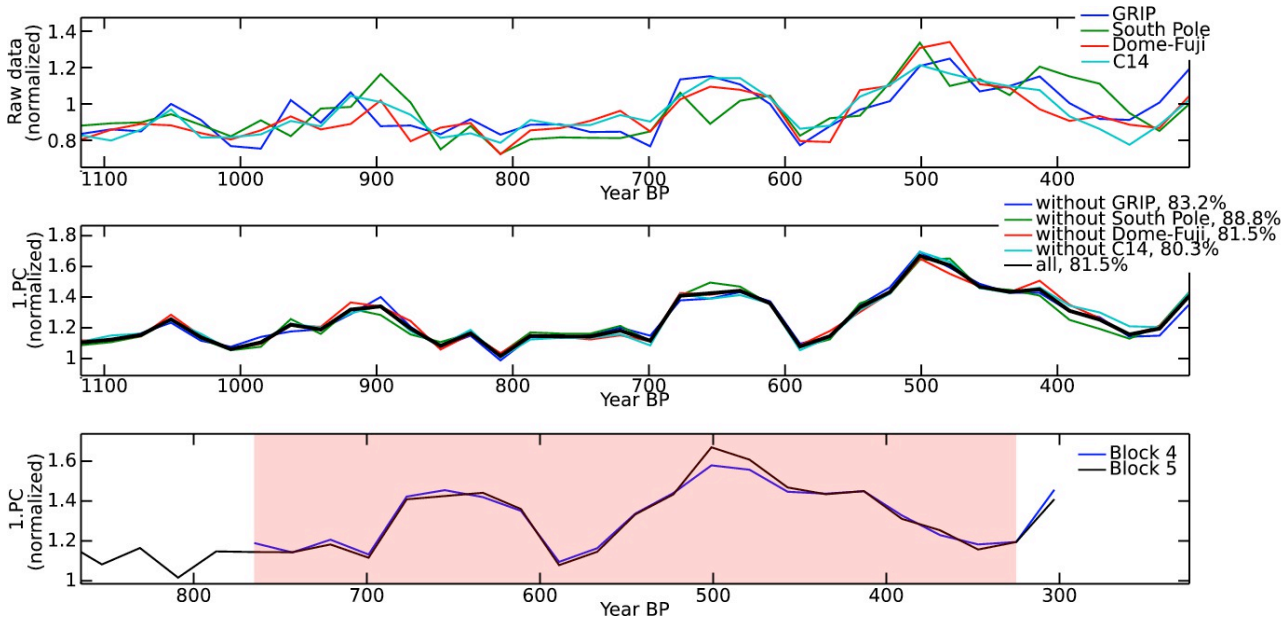

Figure S5 Normalization of block 5. The redish interval is used as normalization period.

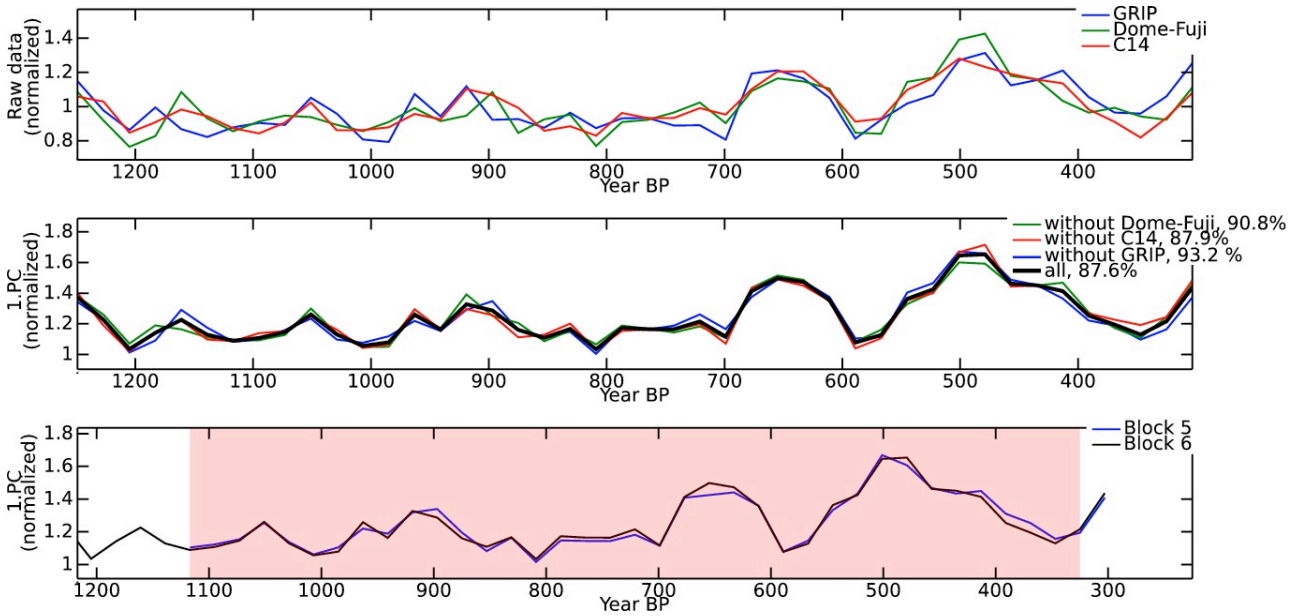

Figure S6 Normalization of block 6. The redish interval is used as normalization period.

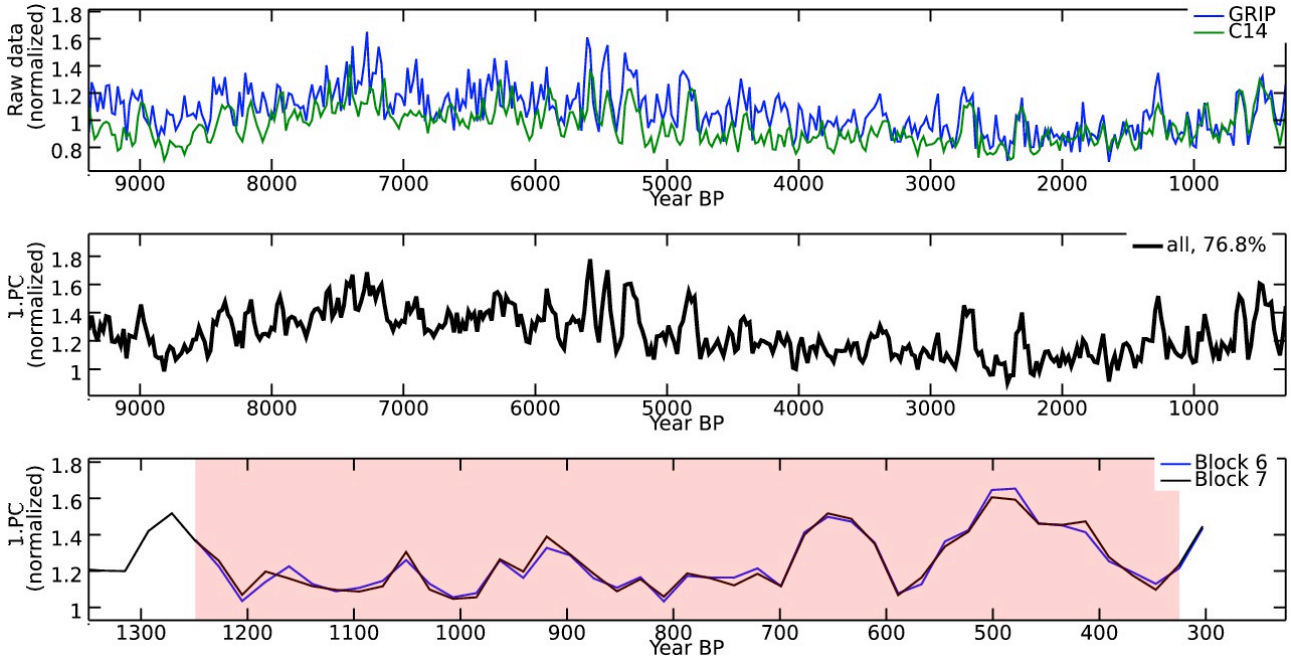

Figure S7 Normalization of block 7. The redish interval is used as normalization period. Note, that in this block jackknife could not be applied because of only two records (GRIP and 14C).

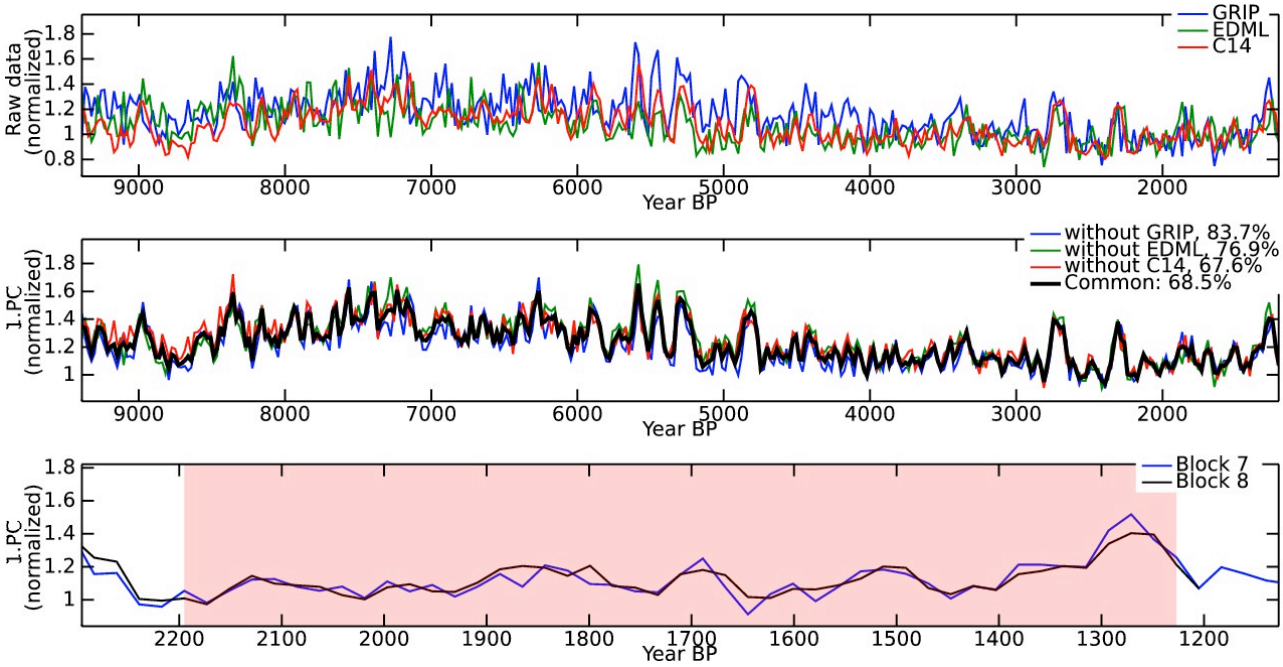

Figure S8 Normalization of block 8. The redish interval is used as normalization period.

S7. Comparison of cosmic ray intensity based on concentrations and fluxes

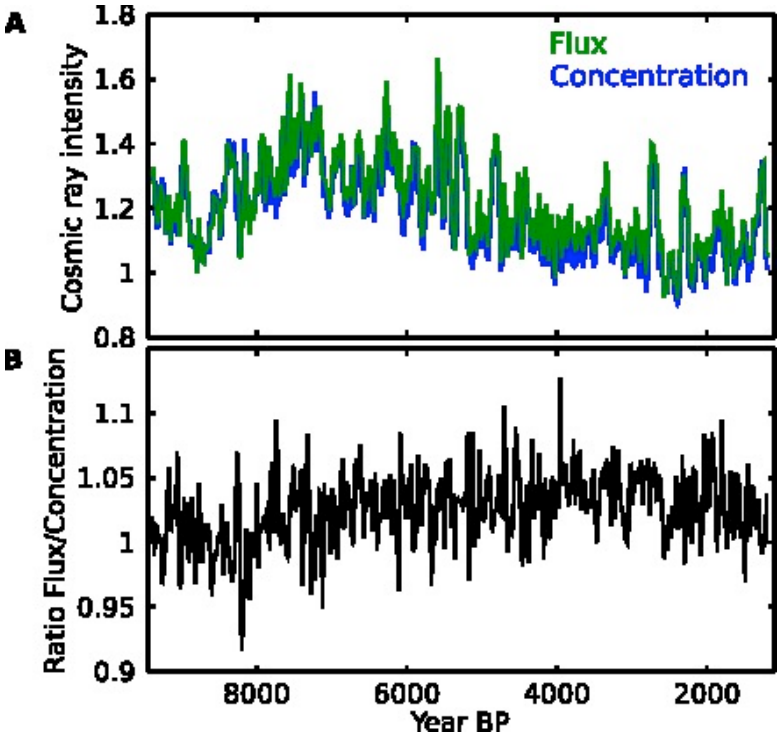

Figure S9: Relative cosmic ray intensity based on the principal component analysis of the radionuclide records averaged over 22 years. Time is given in year BP. **A** *The blue curve is based on ^{10}Be concentrations (EDML and GRIP) and p14C; the green curve is based on ^{10}Be fluxes (EDML and GRIP) and p14C.* **B** *Ratio of flux and concentration based reconstructions of the relative cosmic ray intensity from panel A. The two reconstructions of cosmic ray intensity differ by less than 5% on average.*

S8. Determination of the uncertainty of the cosmic ray record

To determine the robustness of the common production signal, we used the jackknife method, which means we applied PCA by leaving out individual radionuclide records. In every block PCA was done as often as radionuclide records are considered. By doing so every radionuclide record has been left out in one PCA calculation. Therewith, lower and upper curves of the common production signal could be determined. The maximal difference between the lower and upper curves and the production signal, when all radionuclide records are considered, is the herein called maximal jackknife uncertainty. This uncertainty is shown in Figure S10 as a function of time. In addition the standard deviation of the "raw" radionuclide records is shown. Figure S11 shows the corresponding distributions. It can be seen that already the "raw" radionuclide records do differ on average by less than 10 %. The jackknife uncertainty is on average 5 %. As a conservative estimate we use the standard deviation of the "raw" radionuclide records as uncertainty of the final common production rate record (as shown as cosmic ray intensity in Figure 3 B, C, D).

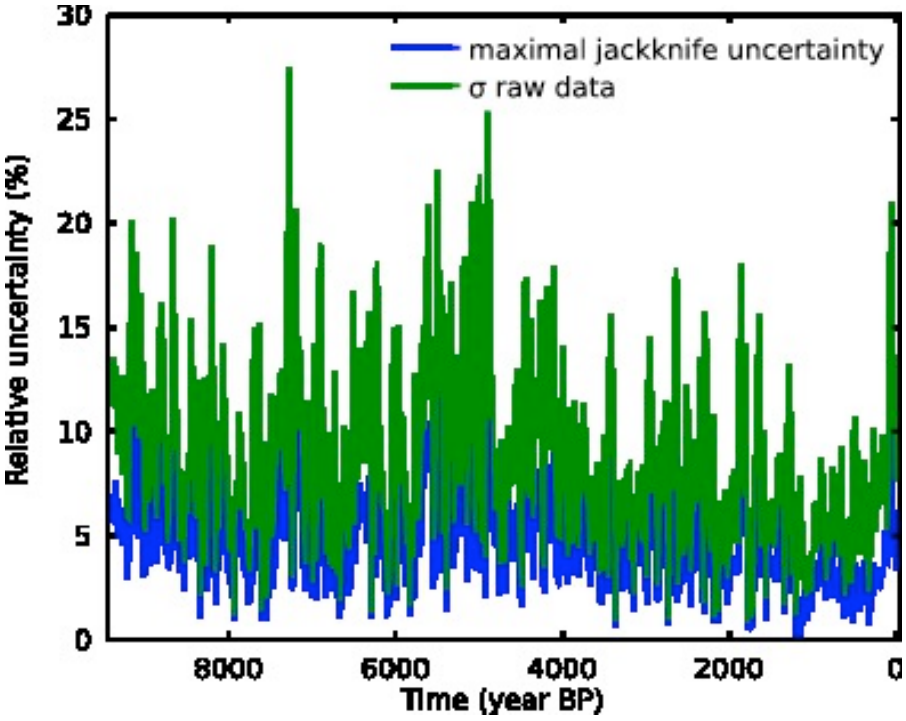

Figure S10: Comparison of uncertainty in time: jackknife method and standard deviation of "raw" radionuclide records. Time is given in year BP.

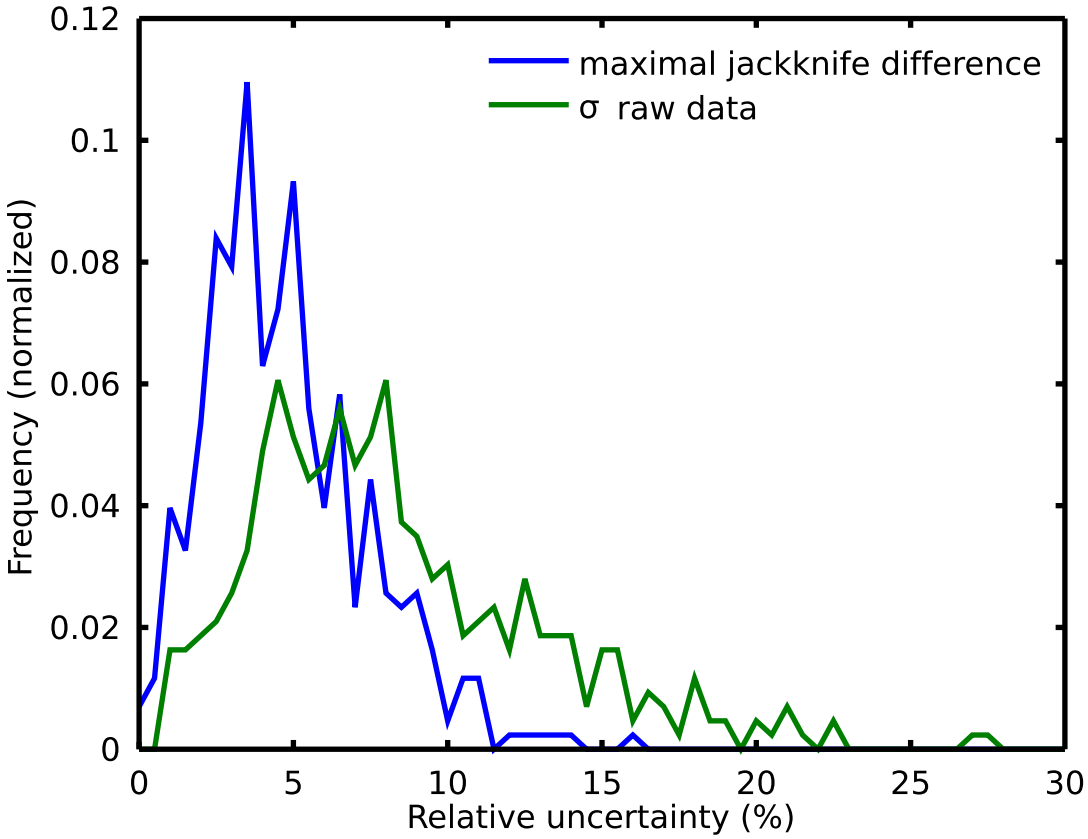

Figure S11: Comparison of uncertainty distribution: jackknife method and standard deviation of "raw" radionuclide records. Distributions are normalized by the integral over all uncertainty bins.

S9. Calculation of ^{10}Be production for the period 1937-2010 from neutron monitor and ionization chamber data

To compare the 9400-year long record of cosmic ray intensity with the most recent years, neutron monitor and ionization chamber data are used to calculate cosmic ray intensity. These data allow determining the solar modulation potential Φ (16). The solar modulation potential Φ is a parameter describing the cosmic ray intensity modulation outside the Earth's magnetic field. The Φ data of (16) are available as monthly means. We averaged the monthly means to 22-year averages equal to the radionuclide records of this study. This Φ record is based on another interstellar spectrum than the production calculation by (1) which has been corrected using the approach described in (17). The 22-year averages of the Φ record were used together with the radionuclide production calculations by (1) to calculate the ^{10}Be production during the instrumental (neutron monitor and ionization chamber) era. Figure S12 compares the ^{10}Be production calculated from the three 22-year average data points of Φ with the common production rate from the radionuclide records. The ^{10}Be production rate calculated for the annual averages of Φ is also shown. Both the radionuclide based and the instrumental based records are normalized for the same period of 1944-1988, and can therefore be directly compared with each other. The reconstructed annual ^{10}Be production rate varies inversely proportional to the 11-year solar cycle with a relative change between solar minima and maximum from 0.8 to 1.2. Multi-decadal variability is practically absent in the recent decades, i.e. the long-term variability of the ^{10}Be production (cosmic ray intensity) has been very low during this period compared with the past 200 years as shown in Fig. S12.

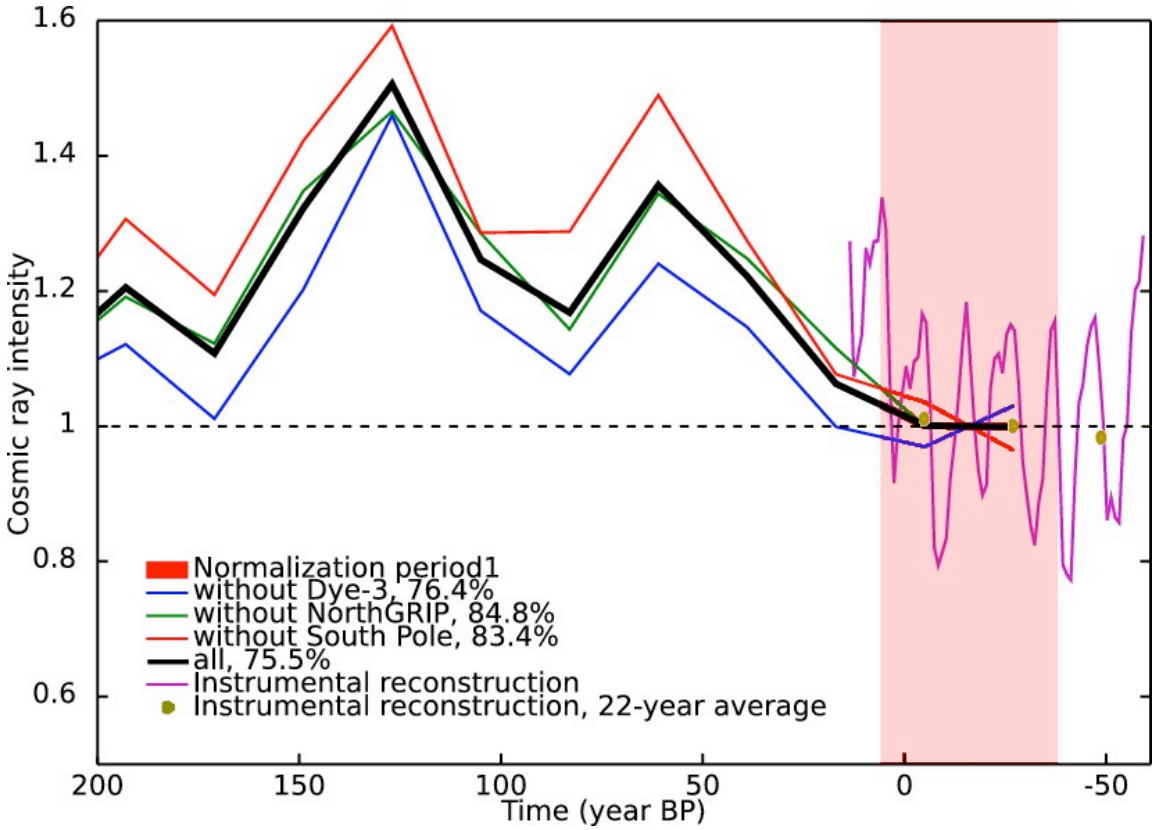

Figure S12: Comparison of cosmic ray intensity obtained with cosmogenic radionuclides and with instrumental data (neutron monitors and ionization chambers). Time is given in year BP. Data are normalized to the period of 1944-1988AD (6 to (-38) BP).

S10. Reconstruction of solar activity (total solar irradiance) from the cosmic ray intensity record

We reconstructed the solar activity (total solar irradiance) from the cosmic ray record using the methods as described in refs.(17-20).

First, we reconstructed the solar modulation potential (21), which is a measure of the solar modulation of the cosmic ray particles by removing the effect of the geomagnetic field (1) based on paleomagnetic data reconstructed in ref. (22). The details of this procedure are described in references (1, 17, 20). The Φ reconstruction is shown in Fig. S13. During some very deep solar minima negative values of Φ occur, which is impossible from the physical point of view. As discussed in ref. (23) different explanations exist for the occurrence of negative values such as the uncertainties in radionuclide records, in radionuclide production calculations, in geomagnetic field strength reconstructions, and in the estimation of the local interstellar spectrum.

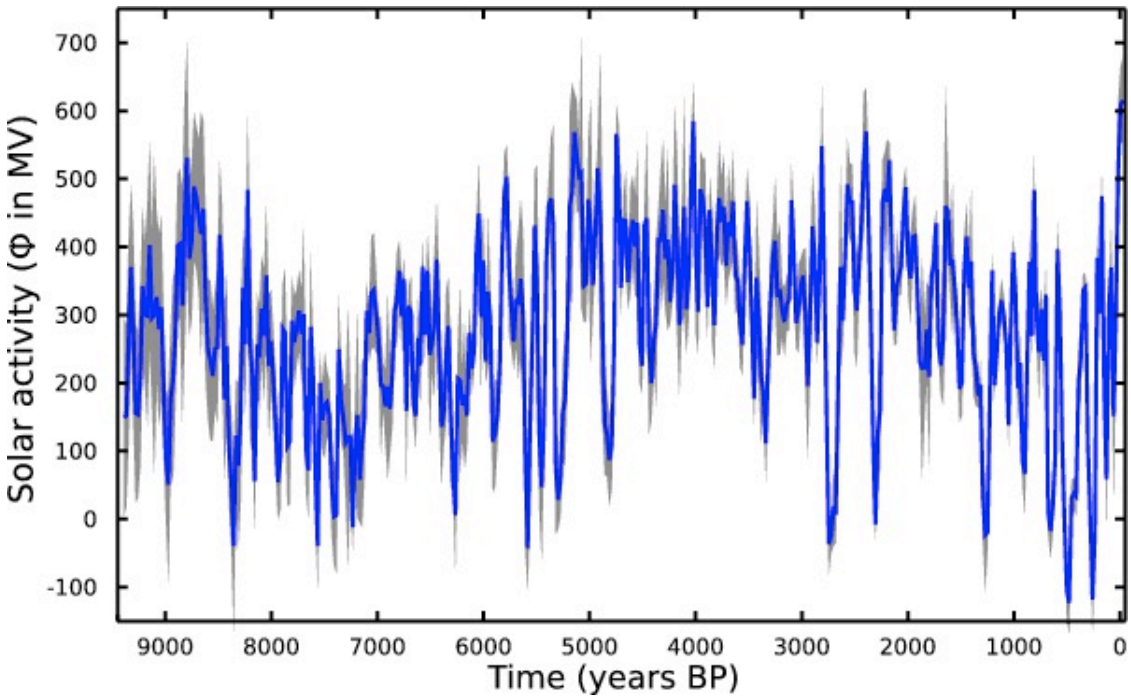

Figure S13 Solar modulation potential Φ reconstructed from the common cosmic ray intensity record. The paleomagnetic field has been removed (22). Φ is calculated with the local interstellar spectrum from ref. (24). Uncertainty is one standard deviation obtained from 1000 Monte Carlo simulations considering uncertainties in cosmic ray record and geomagnetic field strength. Time is given in year BP. Note that the variation on the millennial time-scale of Φ depends on the geomagnetic field. If another geomagnetic field reconstruction like for example ref (25) were used Φ would show another (long-term) trend on millennial time scales.

Then, the strength of the interplanetary magnetic field is calculated using its physical relationship with solar modulation potential Φ as given in refereces (18, 19). Figure S14 shows the reconstructed interplanetary magnetic field for the period 1880 to the present day. Independent reconstructions of the interplanetary magnetic field based on geomagnetic indices (26) are also plotted. As can be seen our reconstruction agrees reasonably well with the ones based on geomagnetic indices.

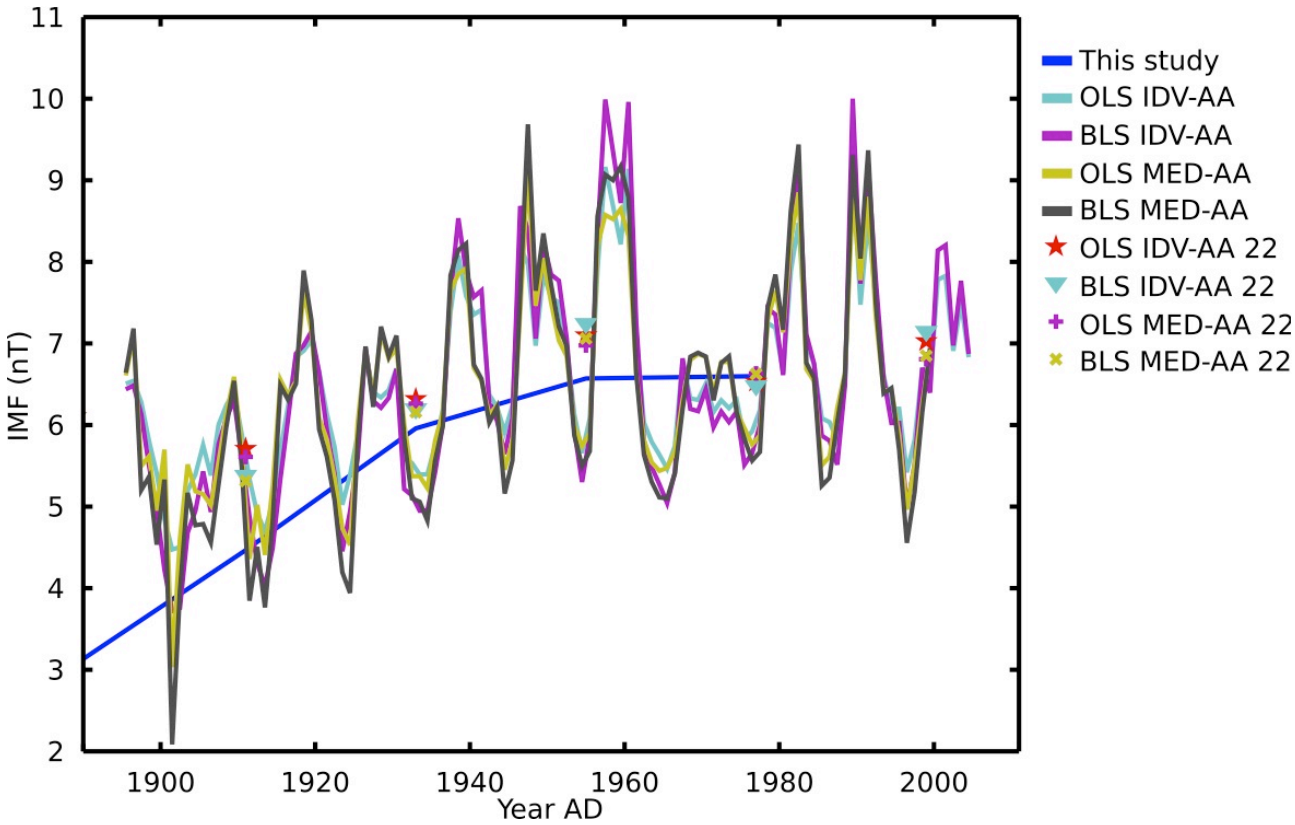

Figure S14 Comparison of interplanetary magnetic field reconstructed from Φ using their physical relationship as given in references (18, 19) (blue curve) with geomagnetic indices based reconstructions (26). The stars, diamonds, pluses, and crosses are 22-year averages of the geomagnetic indices-based reconstructions (same color code as the yearly records).

Third, total solar irradiance is calculated using its observed relationship with the strength of the interplanetary magnetic field (27). The time series of total solar irradiance over the Holocene is shown in Fig. S15. The data set will be available online at the NOAA paleo server (http://www.ncdc.noaa.gov/paleo/forcing.html).

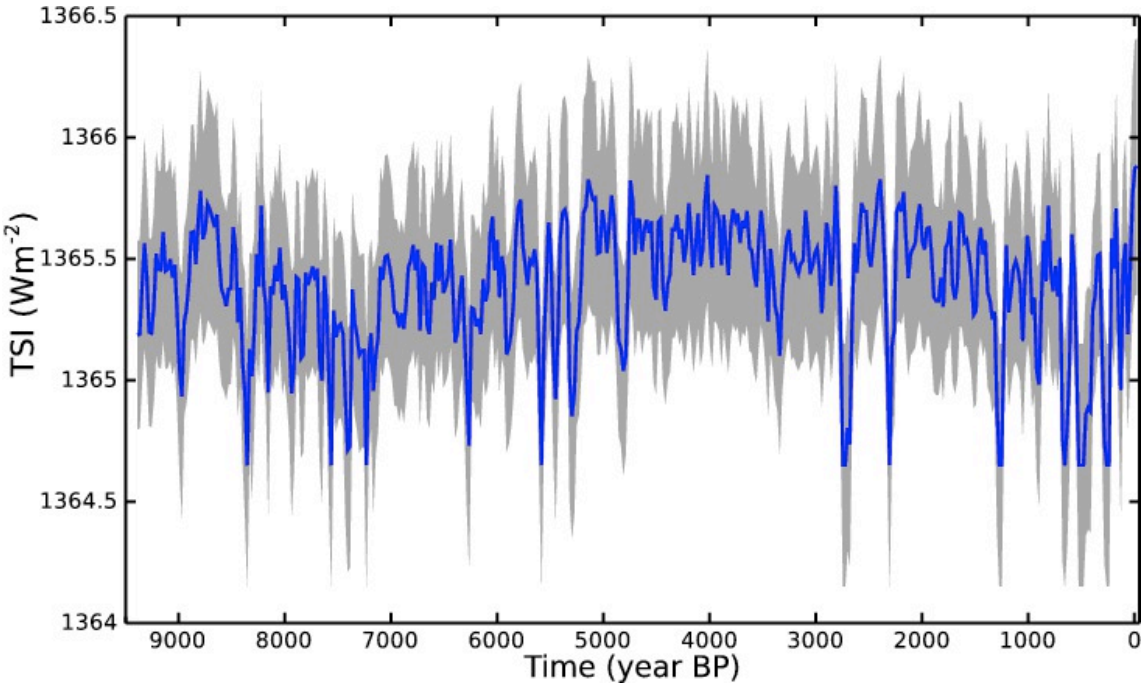

Figure S15 Total solar irradiance calculated using the method given in ref. (19). Time is given in

year BP. Gray shaded uncertainty is one standard deviation obtained from uncertainties in Φ (see Fig. S12), in the relationship of Φ with the interplanetary magnetic field (18, 19), and in the relationship between interplanetary magnetic field and total solar irradiance (27).

S11. Power spectra of total solar irradiance (Figure S16) and $\delta^{18}O$ from Dongge cave

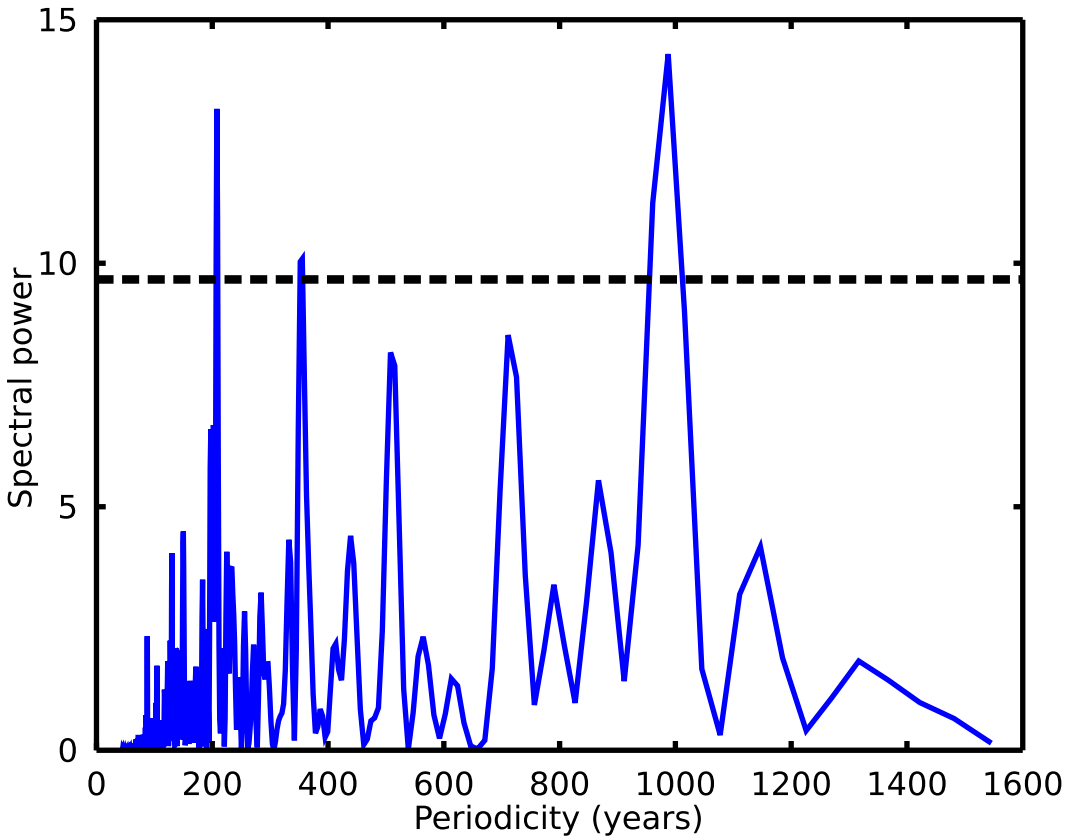

Figure S16 Lomb normalized periodogram (spectral power as a function of periodicity) of total solar irradiance. The horizontal dotted line marks the 95% significance level. Prominent periodicities are the de Vries cycle at ~210 years and the Eddy cycle at ~1000 years (28). These periodicities are used in Fig. 4 of the paper to detect the solar fingerprint in an Asian climate record ($\delta^{18}O$ from Dongge cave, China, (29)). See Figure S17 for periodogram of the climate record.

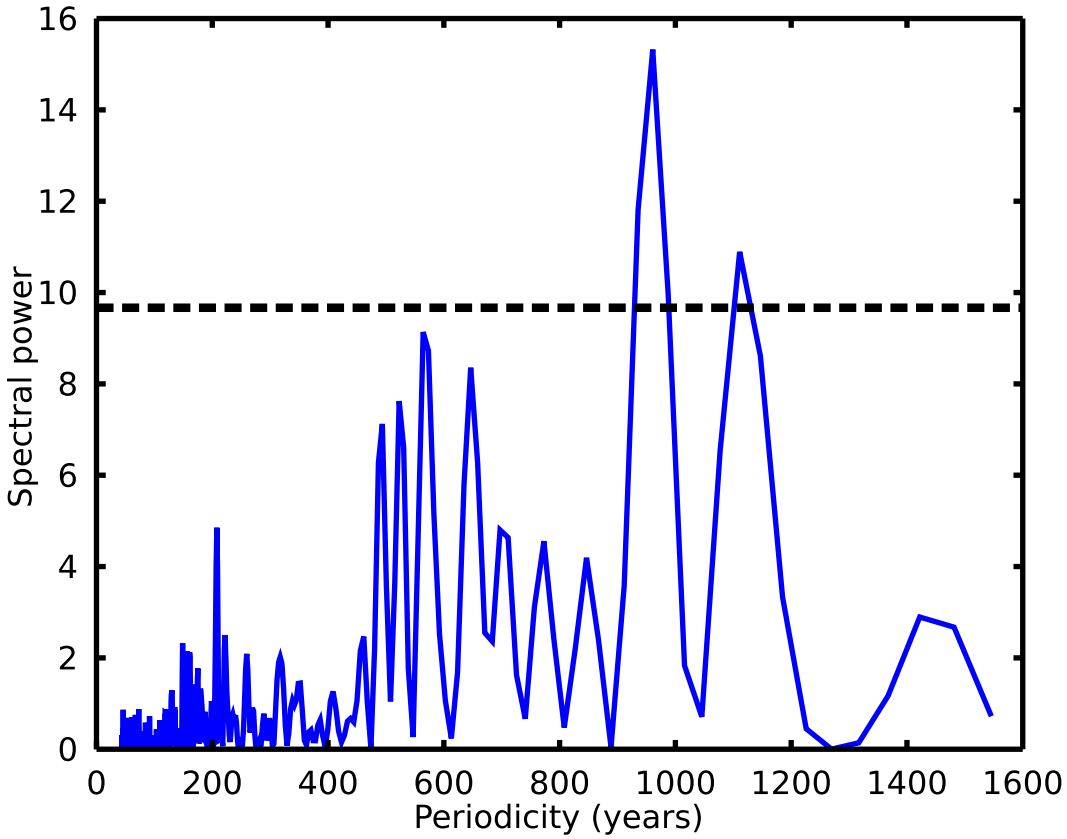

Figure S17 Lomb normalized periodogram (spectral power as a function of periodicity) of the Asian climate record ($\delta^{18}O$) from Dongge cave, China, (29). The horizontal line marks the 95% significance level. Prominent periodicities of solar activity (de Vries cycle at ~210 years and the Eddy cycle at ~1000 years (28)) are found in the climate record (see Figure S16 for periodogram of solar activity). The de Vries cycle is not significant at the 95% level.

S12. Correlation analysis

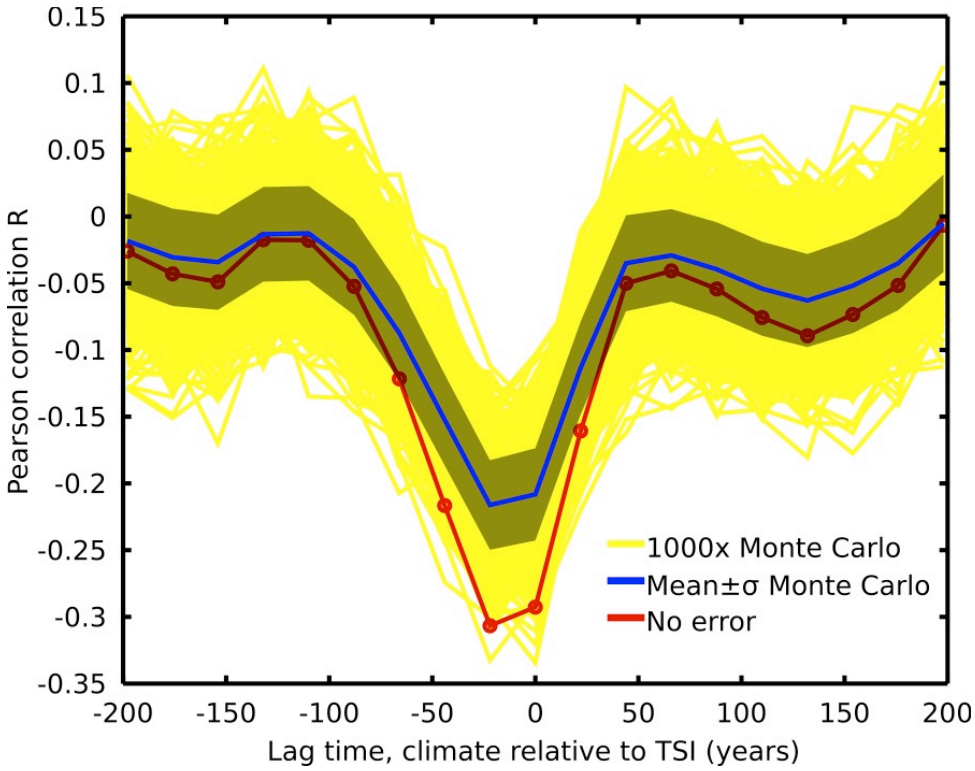

Figure S18 Pearson correlation as a function of lag time between the $\delta^{18}O$ record of Asian monsoon (29) and total solar irradiance (TSI). Both time series are 22-year averages, linearly detrended and high-pass filtered with 2000 years. Lag time is climate time relative to TSI time, i.e. a lag time of 100 years means the climate record lags TSI by 100 years. To consider the uncertainty in the records, we performed 1000 Monte Carlo simulations. For reasons of simplicity we assumed that the time scales in both records and the $\delta^{18}O$ signal have no uncertainty. All uncertainty was put into the TSI signal ($\Delta TSI=1 Wm^{-2}$). The yellow curves in the background show the individual lag correlation curves from the Monte Carlo simulations. The blue curve is the mean value and the standard deviation from the Monte Carlo simulations at individual lag times. The red curve is the result without consideration of any uncertainty (strongest correlation is R=0.31 at the lag time -22 years, the correlation with no lag is R=0.29). The strongest correlation is found for a slightly negative lag time, which is consistent with no lag within the Monte Carlo uncertainty.

S13. Comparison of total solar irradiance (TSI) with published reconstructions

In figures S19 and S20 the time series of total solar irradiance of this study is compared with two existing reconstructions also covering the Holocene. The reconstructions are abbreviated with SEA09 (19) and.with VEA11 (30). SEA09 is based on the ^{10}Be record from GRIP ice core and VEA11 is based on the ^{14}C INTCAL04 record. Both records are used in this paper. In this paper the GRIP time scale is GICC05 whereas the GRIP timescale ss09 is used in SEA09, and that in this paper the updated ^{14}C INTCAL09 record is used instead of INTCAL04 that is used by VEA11. As can be seen from the panels a and b in both figures there is a good agreement between the curves except that the amplitudes of individual grand solar minima are different. The difference between TSI of this study and SEA09/VEA11 (panel b in both figures) show short-term variability but no long-term trend. The panels c in the figures show the wavelet coherence. At short periodicities the coherence has very little power whereas the coherence is high at longer periodicities. This can be explained by the fact that system effects occur mainly on shorter time scales (<100 years). Thus, the wavelet coherence panels clearly point to a noise reduction in the derived TSI record of this study compared to the former records SEA09 and VEA11 which are based on individual radionuclide

records only.

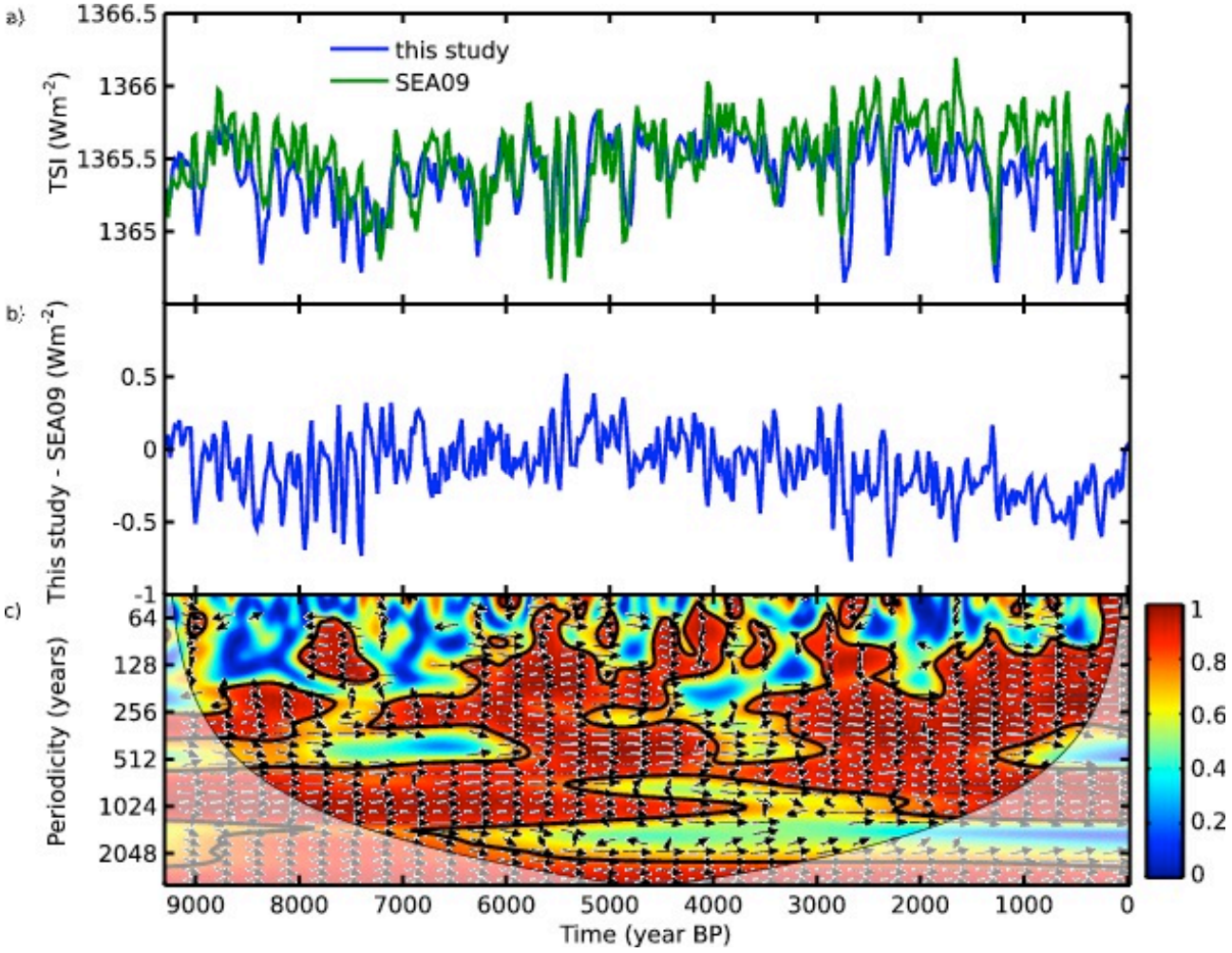

Figure S19 Comparison of TSI of this study with SEA09 (19). Time is given in year BP. a) Time series of TSI of this study (blue) and SEA09 (green). SEA09 was averaged to 22 years to be comparable with TSI of this study. b) Difference. c) Wavelet coherence. Arrows pointing to the right are in phase. Black boundaries mark regions with 95% significance.

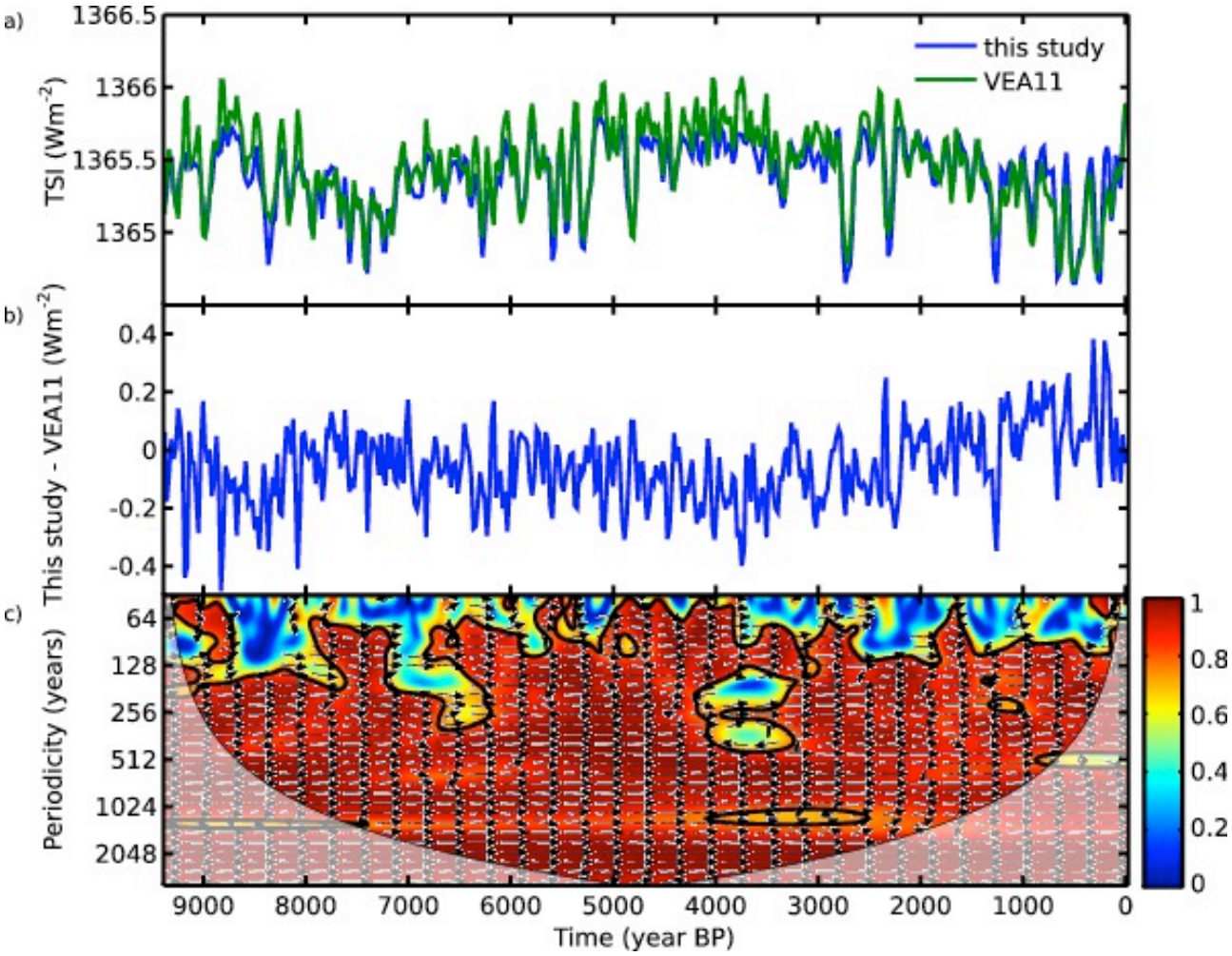

Figure S20 Comparison of TSI of this study with VEA11 (30). Time is given in year BP. a) Time series of TSI of this study (blue) and VEA11 (green). VEA11 are originally 10-year averages and was averaged to 22 years to be comparable with TSI of this study. b) Difference. c) Wavelet coherence. Arrows pointing to the right indicate that the data are in phase. Black boundaries mark regions with 95% significance.

References

1. *Masarik J & Beer J (2009) An updated simulation of particle fluxes and cosmogenic nuclide production in the Earth's atmosphere. J Geophys Res-Atmos 114:D11103.*
2. *Reimer PJ, et al. (2009) Intcal09 and Marine09 Radiocarbon Age Calibration Curves, 0-50,000 Years Cal Bp. Radiocarbon 51(4):1111-1150.*
3. *Yiou F, et al. (1997) Beryllium 10 in the Greenland Ice Core Project ice core at Summit, Greenland. J Geophys Res-Oceans 102(C12):26783-26794.*
4. *Muscheler R, et al. (2004) Changes in the carbon cycle during the last deglaciation as indicated by the comparison of Be-10 and C-14 records. Earth Planet Sc Lett 219(3-4):325-340.*
5. *Beer J, Tobias S, & Weiss N (1998) An active sun throughout the Maunder Minimum. Sol Phys 181(1):237-249.*
6. *Beer J, et al. (1985) Accelerator Measurements of Be-10 - the 11 Year Solar-Cycle from 1180-1800 Ad. Nucl Instrum Meth B 10-1(MAY):415-418.*
7. *Berggren AM, et al. (2009) A 600-year annual Be-10 record from the NGRIP ice core,*

Greenland. Geophys Res Lett 36:L11801.

8. *Raisbeck GM, Yiou F, Jouzel J, & Petit JR (1990) Be-10 and Delta-H-2 in Polar Ice Cores as a Probe of the Solar Variability Influence on Climate. Philos T Roy Soc A 330(1615):463-470.*
9. *Horiuchi K, et al. (2008) Ice core record of Be-10 over the past millennium from Dome Fuji, Antarctica: A new proxy record of past solar activity and a powerful tool for stratigraphic dating. Quat Geochronol 3(3):253-261.*
10. *Epica Community Members (2006) One-to-one coupling of glacial climate variability in Greenland and Antarctica. Nature 444(7116):195-198.*
11. *Kubik PW & Christl M (2010) Be-10 and Al-26 measurements at the Zurich 6 MV Tandem AMS facility. Nucl Instrum Meth B 268(7-8):880-883.*
12. *Ruth U, et al. (2007) "EDML1": a chronology for the EPICA deep ice core from Dronning Maud Land, Antarctica, over the last 150 000 years. Clim Past 3(3):475-484.*
13. *Korschinek G, et al. (2010) A new value for the half-life of Be-10 by Heavy-Ion Elastic Recoil Detection and liquid scintillation counting. Nucl Instrum Meth B 268(2):187-191.*
14. *Chmeleff J, von Blanckenburg F, Kossert K, & Jakob D (2010) Determination of the Be-10 half-life by multicollector ICP-MS and liquid scintillation counting. Nucl Instrum Meth B 268(2):192-199.*
15. *Siegenthaler U (1983) Uptake of Excess CO_2 by an Outcrop-Diffusion Model of the Ocean. J Geophys Res-Oc Atm 88(NC6):3599-3608.*
16. *Usoskin IG, Bazilevskaya GA, & Kovaltsov GA (2011) Solar modulation parameter for cosmic rays since 1936 reconstructed from ground-based neutron monitors and ionization chambers. J Geophys Res-Space 116:A02104.*
17. *Steinhilber F, Abreu J, & Beer J (2008) Solar modulation during the Holocene. Astrophysics and Space Sciences Transactions 4(1):1-6.*
18. *Steinhilber F, Abreu JA, Beer J, & McCracken KG (2010) Interplanetary magnetic field during the past 9300 years inferred from cosmogenic radionuclides. J Geophys Res-Space 115:A01104.*
19. *Steinhilber F, Beer J, & Frohlich C (2009) Total solar irradiance during the Holocene. Geophys Res Lett 36:L19704.*
20. *Vonmoos M, Beer J, & Muscheler R (2006) Large variations in Holocene solar activity: Constraints from Be-10 in the Greenland Ice Core Project ice core. J Geophys Res-Space 111(A10):A10105.*
21. *Gleeson LJ & Axford WI (1968) Solar Modulation of Galactic Cosmic Rays. Astrophys J 154(3P1):1011-1026.*
22. *Knudsen MF, et al. (2008) Variations in the geomagnetic dipole moment during the Holocene and the past 50 kyr. Earth Planet Sc Lett 272(1-2):319-329.*
23. *Herbst K, et al. (2010) On the importance of the local interstellar spectrum for the solar modulation parameter. J Geophys Res-Atmos 115:-.*
24. *Garciamunoz M, Mason GM, & Simpson JA (1975) Anomalous He-4 Component in Cosmic-Ray Spectrum at Less Than Equal to 50 Mev Per Nucleon during 1972-1974. (Translated from English) Astrophys J 202(1):265-275 (in English).*
25. *Korte M & Constable CG (2005) The geomagnetic dipole moment over the last 7000 years - new results from a global model. Earth Planet Sc Lett 236(1-2):348-358.*

26. *Rouillard AP, Lockwood M, & Finch I (2007) Centennial changes in the solar wind speed and in the open solar flux. (Translated from English) J Geophys Res-Space 112(A5):- (in English).*

27. *Frohlich C (2009) Evidence of a long-term trend in total solar irradiance. Astron Astrophys 501(3):L27-U508.*

28. *Abreu JA, Beer J, & Ferriz-Mas A (2010) Past and future solar activity from cosmogenic radionuclides. Astronomical society of the pacific conference series: SOHO-23: Understanding a peculiar solar minimum, Editors: S.R. Cranmer, J.T. Hoeksema, J.L. Kohl 428.*

29. *Wang YJ, et al. (2005) The Holocene Asian monsoon: Links to solar changes and North Atlantic climate. Science 308(5723):854-857.*

30. *Vieira LEA, Solanki SK, Krivova N, & Usoskin I (2011) Evolution of the solar irradiance during the Holocene Astron Astrophys.*